

A 99-Line Homogenization Code for Lattice-skin Plate Structures

Zhongkai Ji¹, Dawei Li^{2*}, Yong Zhao^{1*}, Wenhe Liao²

¹Shanghai Key Laboratory of Digital Manufacture for Thin-Walled Structures, Shanghai Jiao Tong University, Shanghai, 200240, PR China.

²School of Mechanical Engineering, Nanjing University of Science and Technology, Nanjing, 210094, PR China.

*Corresponding author(s). E-mail(s): ldw@njust.edu.cn;
yongzhao@sjtu.edu.cn;

Abstract

Recent years have seen growing application potential for Lattice-skin Plate Structures in advanced manufacturing fields such as aerospace and automotive engineering. For multiscale performance evaluation of such structures, conventional homogenization methods for lattice-filled volume structures are often used for equivalent analysis. However, in finite-thickness Lattice-skin Plate Structures, periodic boundary conditions imposed along the three orthogonal directions of the representative cell cannot adequately capture the boundary effect of the free surfaces in the thickness direction, which introduces bias into the prediction of effective properties. To reduce this bias, this study develops and open-sources a homogenization method for Lattice-skin Plate Structures, forming an open-source computational framework for this class of structures. Representative numerical examples show that the framework can stably extract effective plate/shell stiffness matrices and can be extended to predict multiphase material properties and analyze steady-state heat conduction. The tool provides an open and reusable analysis foundation for the high-fidelity design of multifunctional lightweight structures.

Keywords: Homogenization, Size effect, Lattice-skin plate structures, Open-source code, GPU-accelerated computing

1 Introduction

As a new class of lightweight structures, Lattice-skin Plate Structures show application potential in advanced manufacturing fields such as aerospace(Khan and Riccio 2024; Sun et al. 2025) and automotive engineering(Wang et al. 2025). For performance evaluation of such multiscale structures, the homogenization method for lattice-filled volume structures (LVS-H) is commonly used for multiscale dimensional reduction analysis(Bishara et al. 2023). As skin-enabled structures continue to become thinner, LVS-H may introduce free-surface truncation errors when applied to finite-thickness structures, which leads to bias in the extracted effective mechanical properties(Yi et al. 2015). This is because LVS-H imposes periodic boundary conditions along the three orthogonal directions of the representative volume element (RVE). The mathematical assumption of periodic continuation in the volume does not adequately reflect the free-surface mechanical state through the thickness of a thin plate, and may therefore overestimate the tensile and bending stiffness of the structure(Cai et al. 2014).

To reduce the bias in effective-property prediction for thin plates, the homogenization method for Lattice-skin Plate Structures (LPS-H) has been developed. In the analysis of composites and thin-walled structures, LPS-H preserves free boundary conditions in the out-of-plane normal direction and can characterize plate/shell responses such as extension-bending and extension-twist coupling(Cai et al. 2014; Qiao et al. 2021; Zhou 2025). However, for finite-thickness Lattice-skin Plate Structures with complex topological porosity, LVS-H is still commonly used at present.

Meanwhile, in computational mechanics and structural optimization, open-source programs and educational papers play an important supporting role in the dissemination of technical methods and the development of new algorithms. For example, volume homogenization methods for analyzing the effective elastic tensors of two-dimensional (2D)(Andreassen and Andreassen 2014) and three-dimensional (3D) structures(Dong et al. 2019), together with foundational codes for structural topology optimization(Sigmund 2001; Zhou and Sigmund 2021; Woldseth et al. 2024; Ding 2025), have been used in many follow-up studies(Han and Wei 2022; Gao et al. 2023; Bayat et al. 2023; Zheng et al. 2023) and have provided a basis for secondary development of related algorithms. Motivated by these efforts, the present work provides a compact and efficient open-source framework implementing LPS-H, as shown in **Figure 1**, to supplement the open-source tools available for the mechanical analysis of Lattice-skin Plate Structures. This framework introduces loop-free multidimensional tensor mapping and graphics processing unit (GPU) heterogeneous acceleration, and serves as a core computational tool for the high-fidelity mechanical evaluation and design of multifunctional lightweight Lattice-skin Plate Structures.

2 Theoretical Frameworks for LPS-H

This section first briefly reviews the macroscopic characterization of plate/shell mechanical properties and then compares the theoretical differences between LVS-H and LPS-H in predicting the effective stiffness of complex Lattice-skin Plate Structures, thereby establishing the mathematical basis for the open-source implementation presented later.

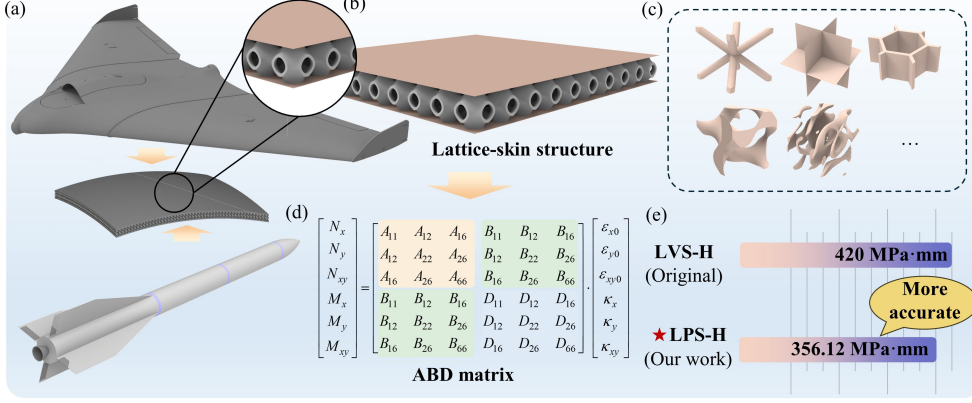


Fig. 1 Open-source LPS-H analysis framework for Lattice-skin Plate Structures. (a,b) Typical applications of Lattice-skin Plate Structures in aerospace fields such as aircraft wings and missile shells. (c) Lightweight Lattice-skin Plate Structures with multiple configurations. (d) Definition of the plate/shell ABD stiffness matrix. (e) Comparison of LPS-H and LVS-H in the prediction of macroscopic effective stiffness.

2.1 Macroscopic plate mechanics and the ABD stiffness matrix

In solid mechanics analysis, full-scale modeling of Lattice-skin Plate Structures with complex internal porosity using a high-fidelity 3D finite element model usually leads to high computational cost (Zhang et al. 2023; Yang et al. 2026). Therefore, replacing the detailed structure with an equivalent macroscopic homogeneous plate/shell is a common dimensional-reduction strategy in engineering practice, as shown in **Figure 2a**. To achieve this cross-scale mechanical equivalence, the basic relation between 3D continuum mechanics and macroscopic plate/shell mechanics must be clarified.

Within the framework of Classical Laminate Plate Theory (CLPT) or First-Order Shear Deformation Theory (FSDT), the macroscopic kinematics of a plate/shell are mainly governed by deformation of the mid-surface. Under the plane-section assumption, the in-plane strain component $\boldsymbol{\varepsilon}(z)$ at an arbitrary point located at the normal coordinate z from the geometric mid-surface can be expressed as the linear superposition of mid-surface membrane deformation and shear, together with bending and twisting deformation:

$$\boldsymbol{\varepsilon}(z) = \boldsymbol{\varepsilon}^0 + z\boldsymbol{\kappa} \quad (1)$$

Here, $\boldsymbol{\varepsilon}^0 = [\varepsilon_{11}^0, \varepsilon_{22}^0, \gamma_{12}^0]^T$ denotes the mid-surface membrane strain and describes the in-plane stretching and shear of the plate/shell. Likewise, $\boldsymbol{\kappa} = [\kappa_{11}, \kappa_{22}, \kappa_{12}]^T$ denotes the mid-surface curvature and describes the out-of-plane bending and twisting of the plate/shell.

For a thin plate under plane stress, the linear elastic constitutive relation between the local microscopic in-plane stress $\boldsymbol{\sigma}_p = [\sigma_{11}, \sigma_{22}, \sigma_{12}]^T$ and the local strain $\boldsymbol{\varepsilon}(z)$ is governed by the reduced plane-stress stiffness matrix $\mathbf{Q}(z)$:

$$\boldsymbol{\sigma}_p(z) = \mathbf{Q}(z)\boldsymbol{\varepsilon}(z) = \mathbf{Q}(z)(\boldsymbol{\varepsilon}^0 + z\boldsymbol{\kappa}) \quad (2)$$

At the macroscopic level, the internal resultants of the plate/shell are obtained by integrating the local in-plane stress $\boldsymbol{\sigma}_p$ through the physical thickness h , from $z = -h/2$ to $z = h/2$, which yields the equivalent membrane force \mathbf{N} and bending moment \mathbf{M} :

$$\mathbf{N} = \int_{-h/2}^{h/2} \boldsymbol{\sigma}_p(z) dz, \quad \mathbf{M} = \int_{-h/2}^{h/2} \boldsymbol{\sigma}_p(z) z dz \quad (3)$$

Substituting Eq. (2) into the integral expression in Eq. (3), and then separating the mid-surface deformation components $\boldsymbol{\varepsilon}^0$ and $\boldsymbol{\kappa}$ that are independent of the coordinate z , leads to the main constitutive equation relating macroscopic resultants to deformation:

$$\begin{bmatrix} \mathbf{N} \\ \mathbf{M} \end{bmatrix} = \begin{bmatrix} \int \mathbf{Q}(z) dz & \int \mathbf{Q}(z) z dz \\ \int \mathbf{Q}(z) z dz & \int \mathbf{Q}(z) z^2 dz \end{bmatrix} \begin{bmatrix} \boldsymbol{\varepsilon}^0 \\ \boldsymbol{\kappa} \end{bmatrix} = \begin{bmatrix} \mathbf{A} & \mathbf{B} \\ \mathbf{B} & \mathbf{D} \end{bmatrix} \begin{bmatrix} \boldsymbol{\varepsilon}^0 \\ \boldsymbol{\kappa} \end{bmatrix} \quad (4)$$

The 6×6 generalized stiffness matrix in Eq. (4) is called the **ABD** matrix, as shown in **Figure 2b**. It provides a unified basis for evaluating the effective mechanical properties of anisotropic plate/shells. The physical meanings of its submatrices are as follows:

- **A matrix**, of size 3×3 , is the in-plane membrane stiffness matrix. By definition, $\mathbf{A} = \int \mathbf{Q} dz$ establishes the relation between the in-plane membrane force \mathbf{N} and the mid-surface membrane strain $\boldsymbol{\varepsilon}^0$, and characterizes the overall resistance of the plate/shell to in-plane tension, compression, and shear, as shown in **Figure 2d**. Here, A_{11} and A_{22} correspond to the in-plane tensile stiffnesses along the two principal directions, A_{66} represents the in-plane shear stiffness, and A_{12} reflects the Poisson-type coupling between orthogonal directions. For isotropic or orthotropic plate/shells, A_{16} and A_{26} are usually zero. In metamaterial structures with directional or chiral topologies, however, these off-diagonal terms may remain nonzero, meaning that axial stretching can induce in-plane shear deformation, i.e., extension-shear coupling.
- **D matrix**, of size 3×3 , is the out-of-plane bending-torsion stiffness matrix. By definition, $\mathbf{D} = \int \mathbf{Q} z^2 dz$ establishes the relation between the bending moment \mathbf{M} and the curvature $\boldsymbol{\kappa}$, and characterizes the resistance of the plate/shell to out-of-plane bending and twisting. Because this matrix involves a second-order integral with respect to the thickness coordinate z , its value is sensitive to the distribution of material relative to the neutral surface. Therefore, truncation or loss of surface material in thin-walled Lattice-skin Plate Structures often affects the bending-torsion stiffness, as shown in **Figure 2f**. Here, D_{11} and D_{22} denote the bending stiffnesses along the two principal directions, D_{66} denotes the out-of-plane torsional stiffness, and D_{12} describes transverse coupling during bending. Nonzero D_{16} and D_{26} correspond to bending-twist coupling, indicating that bending about a single direction may be accompanied by twisting deformation.
- **B matrix**, of size 3×3 , is the extension-bending coupling stiffness matrix. By definition, $\mathbf{B} = \int \mathbf{Q} z dz$ is the first moment of stiffness through the thickness and reflects

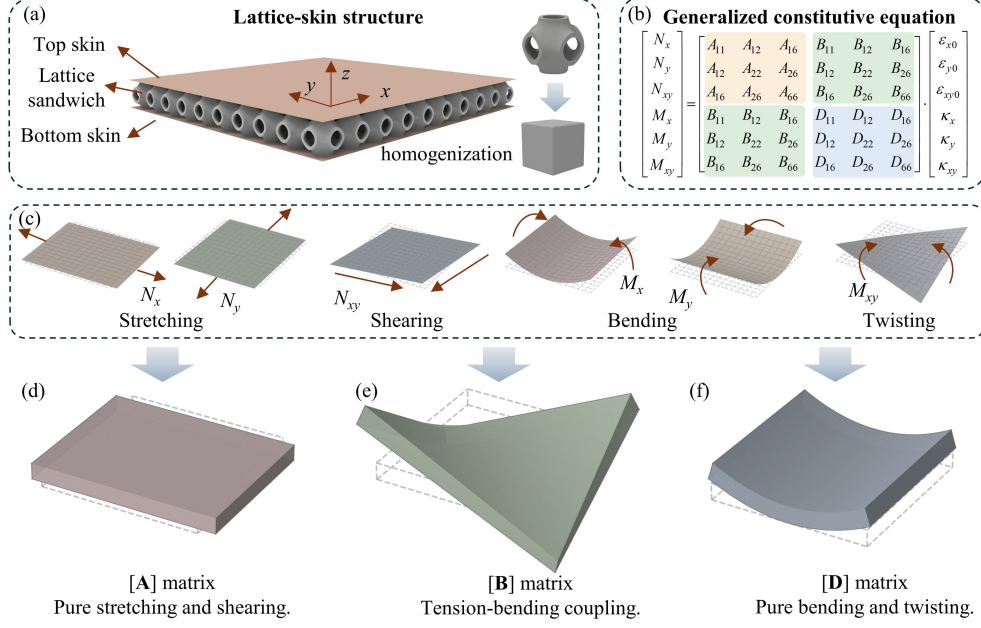


Fig. 2 Equivalent plate/shell mechanical characterization of Lattice-skin Plate Structures and schematic illustration of the ABD stiffness matrix. (a) Dimensional reduction from a Lattice-skin Plate Structure to an equivalent homogeneous plate/shell. (b) Composition and definition of the ABD stiffness matrix. (c) Six basic loading forms used to extract the effective stiffness components. (d-f) Physical meanings of the stiffness components in the **A**, **B**, and **D** matrices.

the coupling between the mid-surface membrane strain ε^0 and the bending moment \mathbf{M} , as well as between the curvature $\boldsymbol{\kappa}$ and the membrane force \mathbf{N} , as shown in **Figure 2e**. For plate/shells with a symmetric material distribution through the thickness, the contributions at positive and negative z cancel each other, so the **B** matrix vanishes. By contrast, in thin-walled metamaterials with thickness-wise asymmetry, a material distribution offset from the mechanical neutral surface introduces eccentricity effects. As a result, a purely in-plane load may induce macroscopic bending, and pure bending may also be accompanied by a membrane-force response. Here, B_{11} , B_{22} , and B_{12} mainly describe extension-bending coupling, whereas B_{16} and B_{26} correspond to extension-twist coupling. The latter is particularly important in Lattice-skin Plate Structures with spatial helices, inclined networks, or asymmetric truncation features, and may lead to macroscopic twisting under uniaxial tension.

For plate/shells whose stiffness distribution is symmetric about the mid-surface, the contributions at positive and negative thickness coordinates in $\mathbf{B} = \int \mathbf{Q}zdz$ cancel each other, so **B** reduces to a zero matrix. For Lattice-skin Plate Structures that contain only a finite number of unit cells through the thickness and are affected by free-surface truncation, however, asymmetry in geometry and material distribution may induce in-plane/out-of-plane coupling responses.

2.2 LVS-H and static condensation

LVS-H originates from classical three-dimensional asymptotic homogenization theory and is commonly used to extract the effective mechanical properties of metamaterials, porous media, and composites. This method treats the RVE with complex microstructural geometry as an equivalent solid that is periodically extended in three-dimensional space. In computation, three-dimensional periodic boundary conditions (3D-PBC) are imposed along the three orthogonal directions, including the thickness direction. The microscale fluctuating displacement fields induced by six independent macroscopic strains are then solved, yielding the effective 6×6 three-dimensional elastic constitutive tensor \mathbf{C}^H .

To use these effective 3D solid properties within the macroscopic plate/shell mechanics framework given by Eq. (4), an additional reduction in dimensionality is required. A macroscopic thin plate mainly carries in-plane loads and out-of-plane bending. Its upper and lower surfaces are usually free boundaries, so the plane-stress condition can be approximated, namely $\sigma_{33} \approx 0$. Transverse shear stresses, which are only weakly related to the membrane-bending response of the plate/shell, can also be neglected in this framework. Based on these assumptions, the traditional treatment usually employs static condensation to reduce the 6×6 effective 3D stiffness matrix \mathbf{C}^H to the 3×3 effective plane-stress stiffness matrix \mathbf{Q}^H .

Specifically, under the constraint $\sigma_{33} = 0$, the out-of-plane normal strain ε_{33} can be expressed as a function of the in-plane strain components and substituted back into the 3D constitutive equation, thereby eliminating the normal degree of freedom. The resulting analytical relation between the matrix entries Q_{ij}^H of \mathbf{Q}^H and the effective 3D stiffness components C_{ij}^H can be written as

$$Q_{ij}^H = C_{ij}^H - \frac{C_{i3}^H C_{j3}^H}{C_{33}^H} \quad (i, j = 1, 2, 6) \quad (5)$$

After this reduced stiffness matrix has been obtained, the dimensional-reduction procedure in LVS-H substitutes it into the macroscopic integral formulas derived in the previous subsection. At this stage, the microscopic metamaterial is assumed, at the macroscopic level, to be a homogeneous continuum uniformly smeared through the thickness. Analytical integration of the matrix \mathbf{Q}^H over the physical plate thickness h then gives the effective in-plane, extension-bending coupling, and bending stiffness matrices:

$$(\mathbf{A}, \mathbf{B}, \mathbf{D}) = \int_{-h/2}^{h/2} \mathbf{Q}^H(1, z, z^2) dz = \left(\mathbf{Q}^H h, \mathbf{0}, \mathbf{Q}^H \frac{h^3}{12} \right) \quad (6)$$

This treatment, which first extracts effective 3D material properties and then introduces them into the plate/shell constitutive integration, is computationally efficient and convenient to implement, and is therefore common in routine engineering analysis. However, it implicitly assumes periodic continuation through the thickness and uses the effective properties as parameters of a continuous homogeneous material in the macroscopic plate/shell integration. For Lattice-skin Plate Structures that contain only a finite number of unit cells through the thickness, this assumption may deviate from the actual boundary state of the structure. Specifically, the 3D-PBC imposed

through the thickness constrains the microscopic deformation modes of the upper and lower free surfaces, making it difficult to capture the free-surface effect caused by physical truncation.

2.3 LPS-H framework for finite-thickness evaluation

To reduce the mechanical bias introduced by the thickness-wise periodic continuation assumption in LVS-H, especially the stiffness variation and sectional asymmetry caused by truncation of a finite number of unit cells, LPS-H is introduced for finite-thickness plate/shell structures. Starting from the microscopic boundary-value problem, this method considers both the geometric features of the plate/shell and the actual boundary state during homogenization, thereby enabling dimensional reduction from a 3D heterogeneous solid to a 2D equivalent plate/shell model.

In the finite element formulation of LPS-H, the boundary conditions of the RVE are closer to the service boundary state of a thin-walled plate/shell. The method imposes two-dimensional periodic boundary conditions (2D-PBC) only in the in-plane x and y directions to represent periodic continuation in plane. In the out-of-plane thickness direction z , the model retains one-dimensional free boundary conditions (1D-FBC), thereby releasing the kinematic constraints on the upper and lower surfaces. These mixed boundary conditions allow thickness-wise Poisson deformation and local warping under loading, which reduces the stiffness overestimation caused by fully three-dimensional periodic constraints.

Under these mixed boundary conditions, LPS-H extracts the generalized plate/shell stiffness matrix through a finite element algebraic formulation. The procedure can be summarized in the following four steps:

Step 1: The mathematical strategy of column-by-column probing

According to Eq. (4), the unknown **ABD** stiffness matrix is a 6×6 linear mapping operator. It maps the 6-dimensional generalized mid-surface deformation vector $\mathbf{E} = [\boldsymbol{\varepsilon}^0, \boldsymbol{\kappa}]^T$ to the 6-dimensional generalized internal-force response vector $\mathbf{R} = [\mathbf{N}, \mathbf{M}]^T$.

In numerical homogenization, the **ABD** matrix is unknown, so a column-by-column probing strategy is adopted. According to the rule of matrix multiplication, if an orthogonal unit deformation basis vector $\mathbf{E}^{(I)}$ is applied such that only its I th component is equal to 1 and all other components are zero, then the resulting internal-force response vector $\mathbf{R}^{(I)}$ is numerically equal to the I th column of the **ABD** matrix. Therefore, solving the full 6×6 matrix can be converted into solving six independent microscopic response problems under six macroscopic unit deformation modes, where $I = 1, 2, \dots, 6$.

Step 2: Construction of the macroscopic unit deformation modes

To transfer the above 6-dimensional macroscopic unit deformation vector $\mathbf{E}^{(I)}$ to the 3D RVE, it must be decomposed and mapped to the initial local strain at any point inside the RVE. The vector $\mathbf{E}^{(I)}$ can be split into an in-plane membrane part $\boldsymbol{\Lambda}_{mem}^{(I)}$ and an out-of-plane bending part $\boldsymbol{\Lambda}_{bend}^{(I)}$, corresponding to the first three and last three components, respectively:

- **Cases $I = 1, 2, 3$: in-plane membrane strain modes.** Only in-plane tension and shear are activated.

The membrane components take the basis vectors $\mathbf{\Lambda}_{mem}^{(1)} = [1, 0, 0]^T$, $\mathbf{\Lambda}_{mem}^{(2)} = [0, 1, 0]^T$, and $\mathbf{\Lambda}_{mem}^{(3)} = [0, 0, 1]^T$.

The bending components remain zero: $\mathbf{\Lambda}_{bend}^{(1,2,3)} = [0, 0, 0]^T$.

- **Cases $I = 4, 5, 6$: out-of-plane bending and twisting curvature modes.** Only out-of-plane bending and twisting are activated.

The membrane components remain zero: $\mathbf{\Lambda}_{mem}^{(4,5,6)} = [0, 0, 0]^T$.

The bending components take the basis vectors $\mathbf{\Lambda}_{bend}^{(4)} = [1, 0, 0]^T$, $\mathbf{\Lambda}_{bend}^{(5)} = [0, 1, 0]^T$, and $\mathbf{\Lambda}_{bend}^{(6)} = [0, 0, 1]^T$.

Under the plane-section assumption of plate/shell theory, the initial macroscopic strain field $\boldsymbol{\varepsilon}^{macro(I)}(z)$ induced at the point whose normal coordinate from the geometric mid-surface is z inside the RVE can be written in the unified form

$$\boldsymbol{\varepsilon}^{macro(I)}(z) = \mathbf{\Lambda}_{mem}^{(I)} + z\mathbf{\Lambda}_{bend}^{(I)} \quad (7)$$

Step 3: Stress recovery under mixed boundary conditions

After Eq. (7) is applied to the RVE, the initial macroscopic strain field disturbs the local equilibrium of the microscopic solid because the metamaterial contains an interwoven topology of solid matrix and voids. To re-establish equilibrium, the structure develops a local fluctuating displacement field, together with the fluctuating strain $\boldsymbol{\varepsilon}^{fluc(I)}(\mathbf{x})$. By solving the finite element weak form under the mixed boundary conditions of 2D-PBC and 1D-FBC, this fluctuating strain can be obtained, and the microscopic local in-plane stress field $\boldsymbol{\sigma}_p^{(I)}(\mathbf{x})$ for the I th loading case can be recovered from the local constitutive tensor $\mathbf{C}(\mathbf{x})$ of the solid material:

$$\boldsymbol{\sigma}_p^{(I)}(\mathbf{x}) = \mathbf{C}(\mathbf{x}) \left[\boldsymbol{\varepsilon}^{macro(I)}(z) + \boldsymbol{\varepsilon}^{fluc(I)}(\mathbf{x}) \right] \quad (8)$$

Step 4: Area integration and ABD matrix extraction

After obtaining the microscopic stress fields for the six loading cases, LPS-H returns to the physical definition of the macroscopic internal resultants. By taking spatial moment integrals of $\boldsymbol{\sigma}_p^{(I)}(\mathbf{x})$ over the microscopic solid volume domain Ω and dividing by the macroscopic projected area S of the RVE, the macroscopic generalized internal-force vector $\mathbf{R}^{(I)}$ is obtained:

$$\begin{bmatrix} \mathbf{N}^{(I)} \\ \mathbf{M}^{(I)} \end{bmatrix} = \frac{1}{S} \int_{\Omega} \begin{bmatrix} \boldsymbol{\sigma}_p^{(I)}(\mathbf{x}) \\ \boldsymbol{\sigma}_p^{(I)}(\mathbf{x})z \end{bmatrix} d\Omega \quad (9)$$

As described in Step 1, the resulting internal-force vector corresponds numerically to the I th column of the **ABD** matrix. In this way, a mapping is established from microscopic stress integration to macroscopic stiffness components:

- **When $I = 1, 2, 3$, corresponding to in-plane tension and shear cases:** the in-plane membrane force $\mathbf{N}^{(I)}$ obtained from the upper part of the integral

expression forms Columns 1, 2, and 3 of the \mathbf{A} matrix;
the out-of-plane bending moment $\mathbf{M}^{(I)}$ obtained from the lower part forms Columns 1, 2, and 3 of the extension-bending coupling matrix \mathbf{B} .

- **When $I = 4, 5, 6$, corresponding to out-of-plane bending and twisting cases:**

the in-plane membrane force $\mathbf{N}^{(I)}$ obtained from the upper part of the integral expression forms Columns 4, 5, and 6 of the coupling matrix \mathbf{B} ; according to the reciprocity theorem, this block is theoretically symmetric with the \mathbf{B} block obtained in the previous step;

the out-of-plane bending moment $\mathbf{M}^{(I)}$ obtained from the lower part forms Columns 1, 2, and 3 of the bending stiffness matrix \mathbf{D} .

3 Program Structure and Python Implementation

The compact Python open-source code developed for LPS-H is analyzed below. It relies on the standard scientific computing libraries NumPy and SciPy, together with the CuPy library for GPU heterogeneous acceleration. The full program is modularized into four main functions. Following the execution flow of plate/shell finite element homogenization, the main code blocks and their underlying vectorized algorithms are described. The code is available in the open-source repository at [core/plate_homogenizer.py](#).

3.1 Material Definition and Element Stiffness

The first step of the homogenization calculation is to define the constitutive relation of the microscopic base material and the element stiffness matrix of the discretized mesh. In this code, these tasks are implemented by the two functions `get_isotropic_elasticity` and `compute_element_stiffness`.

```

8  def get_isotropic_elasticity(E=1.0, nu=0.3):
9      lam, mu = E * nu / ((1 + nu) * (1 - 2 * nu)), E / (2 * (1 + nu)) #
      Calculate Lamé parameters
10     C = np.zeros((6, 6)) # Initialize 6x6 constitutive matrix
11     C[0:3, 0:3] = lam
12     np.fill_diagonal(C[0:3, 0:3], lam + 2 * mu)
13     np.fill_diagonal(C[3:6, 3:6], mu)
14     return C

```

As shown in Lines 8-14, the program first computes the Lamé constants λ and μ from the input Young's modulus E and Poisson's ratio ν .

$$\lambda = \frac{\nu E}{(1 + \nu)(1 - 2\nu)}, \mu = \frac{E}{2(1 + \nu)} \quad (10)$$

The code then uses NumPy array slicing and the diagonal-filling function `fill_diagonal` to construct the 6×6 constitutive matrix \mathbf{C} for an isotropic linear

elastic material.

$$\mathbf{C} = \lambda \begin{bmatrix} 1 & 1 & 1 & 0 & 0 & 0 \\ 1 & 1 & 1 & 0 & 0 & 0 \\ 1 & 1 & 1 & 0 & 0 & 0 \\ 0 & 0 & 0 & 0 & 0 & 0 \\ 0 & 0 & 0 & 0 & 0 & 0 \\ 0 & 0 & 0 & 0 & 0 & 0 \end{bmatrix} + \mu \begin{bmatrix} 2 & 0 & 0 & 0 & 0 & 0 \\ 0 & 2 & 0 & 0 & 0 & 0 \\ 0 & 0 & 2 & 0 & 0 & 0 \\ 0 & 0 & 0 & 1 & 0 & 0 \\ 0 & 0 & 0 & 0 & 1 & 0 \\ 0 & 0 & 0 & 0 & 0 & 1 \end{bmatrix} \quad (11)$$

After the material constitutive tensor has been obtained, the code discretizes the metamaterial RVE using standard eight-node hexahedral elements.

```

17 def compute_element_stiffness(C, dx, dy, dz):
18     Ke, Bs = np.zeros((24, 24)), []
19     nodes = np.array([[ -1, -1, -1], [ 1, -1, -1], [ 1, 1, -1], [ -1, 1, -1], [ -1,
20     -1, 1], [ 1, -1, 1], [ 1, 1, 1], [ -1, 1, 1]]) # 8-node local coordinates
21     detJ = dx * dy * dz / 8.0
22     for q in nodes / np.sqrt(3): # Loop over 8 Gauss integration points
23         dN = 0.125 * np.array([(1 + q[1] * nodes[:, 1]) * (1 + q[2] * nodes[:,
24         2]) * nodes[:, 0] * (2 / dx), (1 + q[0] * nodes[:, 0]) * (1 + q[2] * nodes
25        [:, 2]) * nodes[:, 1] * (2 / dy), (1 + q[0] * nodes[:, 0]) * (1 + q[1] *
26         nodes[:, 1]) * nodes[:, 2] * (2 / dz)]) # Cartesian derivatives
27         B = np.zeros((6, 24)) # Strain-displacement matrix
28         B[0, 0::3], B[1, 1::3], B[2, 2::3] = dN[0], dN[1], dN[2]
29         B[3, 1::3], B[3, 2::3] = dN[2], dN[1]
30         B[4, 0::3], B[4, 2::3] = dN[2], dN[0]
31         B[5, 0::3], B[5, 1::3] = dN[1], dN[0]
32         Bs.append(B) # Store B matrices for stress recovery
33         Ke += B.T @ C @ B * detJ # Accumulate local stiffness
34     return Ke, Bs, detJ

```

Lines 17-30 show the analytical calculation of the element stiffness matrix \mathbf{K}_e . To evaluate the stiffness matrix on a regular voxel grid, the program introduces an isoparametric mapping from the physical coordinate system (x, y, z) to the dimensionless local natural coordinates $(\xi, \eta, \zeta \in [-1, 1])$. For an orthogonal regular element with side lengths dx , dy , and dz , the Jacobian matrix \mathbf{J} degenerates into a diagonal matrix, and its determinant is constant over the entire element domain:

$$|J| = \det(\mathbf{J}) = \frac{dx}{2} \cdot \frac{dy}{2} \cdot \frac{dz}{2} = \frac{dx \cdot dy \cdot dz}{8} \quad (12)$$

The theoretical definition of the stiffness matrix is the volume integral over the physical domain, $\mathbf{K}_e = \int_{V_e} \mathbf{B}^T \mathbf{C} \mathbf{B} dV$. The code uses a $2 \times 2 \times 2$ Gauss-Legendre quadrature rule to convert this volume integral into a discrete sum over eight integration points:

$$\mathbf{K}_e = \sum_{g=1}^8 \mathbf{B}^T(\mathbf{q}_g) \mathbf{C} \mathbf{B}(\mathbf{q}_g) |J| W_g \quad (13)$$

Because the Gauss-point coordinates in each direction are $\pm 1/\sqrt{3}$ and the corresponding integration weights satisfy $w_i = 1$, the total 3D weight is $W_g = 1 \times 1 \times 1 = 1$. Here, $\mathbf{q}_g = (\xi_g, \eta_g, \zeta_g)$ denotes the coordinates of the eight Gauss points.

For an eight-node hexahedral element, the shape function N_i of Node i is defined as

$$N_i(\xi, \eta, \zeta) = \frac{1}{8} (1 + \xi_i \xi) (1 + \eta_i \eta) (1 + \zeta_i \zeta) \quad (i = 1, \dots, 8) \quad (14)$$

To construct the strain-displacement matrix \mathbf{B} , the derivatives of the shape functions with respect to the physical coordinates (x, y, z) must be computed, which can be written as

$$\frac{\partial N_i}{\partial x} = \frac{\partial N_i}{\partial \xi} \frac{\partial \xi}{\partial x} \quad (15)$$

Because the mapping is linear, the geometric scaling factor is $\frac{\partial \xi}{\partial x} = \frac{2}{dx}$. The array `dN` in Line 22 uses vectorized operations to compute the physical-space derivatives of all eight nodes at the current integration point simultaneously:

$$\begin{bmatrix} \text{dN}[0] \\ \text{dN}[1] \\ \text{dN}[2] \end{bmatrix} = \begin{bmatrix} \frac{\partial N}{\partial \xi} \\ \frac{\partial N}{\partial \eta} \\ \frac{\partial N}{\partial \zeta} \end{bmatrix} = \frac{1}{8} \begin{bmatrix} \xi_i(1 + \eta_i\eta_g)(1 + \zeta_i\zeta_g) \frac{2}{dx} \\ \eta_i(1 + \xi_i\xi_g)(1 + \zeta_i\zeta_g) \frac{2}{dy} \\ \zeta_i(1 + \xi_i\xi_g)(1 + \eta_i\eta_g) \frac{2}{dz} \end{bmatrix}_{1 \times 8} \quad (16)$$

Next, Lines 23-28 arrange ε_{xx} , ε_{yy} , ε_{zz} , γ_{yz} , γ_{xz} , and γ_{xy} according to Voigt notation and assemble the derivative vectors into the 6×24 strain-displacement matrix \mathbf{B} :

$$\mathbf{B} = \begin{bmatrix} \frac{\partial N_1}{\partial x} & 0 & 0 & \dots & \frac{\partial N_8}{\partial x} & 0 & 0 \\ 0 & \frac{\partial N_1}{\partial y} & 0 & \dots & 0 & \frac{\partial N_8}{\partial y} & 0 \\ 0 & 0 & \frac{\partial N_1}{\partial z} & \dots & 0 & 0 & \frac{\partial N_8}{\partial z} \\ 0 & \frac{\partial N_1}{\partial z} & \frac{\partial N_1}{\partial y} & \dots & 0 & \frac{\partial N_8}{\partial z} & \frac{\partial N_8}{\partial y} \\ \frac{\partial N_1}{\partial y} & 0 & \frac{\partial N_1}{\partial x} & \dots & \frac{\partial N_8}{\partial y} & 0 & \frac{\partial N_8}{\partial x} \\ \frac{\partial N_1}{\partial z} & \frac{\partial N_1}{\partial x} & 0 & \dots & \frac{\partial N_8}{\partial z} & \frac{\partial N_8}{\partial x} & 0 \end{bmatrix} \quad (17)$$

In Line 29, the chained matrix multiplication `B.T @ C @ B * detJ` accumulates the stiffness contribution from a single integration point. At the same time, the \mathbf{B} matrix at each Gauss point is stored in the list `Bs`, which preserves the required geometric mapping operators for recovering local fluctuation stresses and computing the \mathbf{D} matrix and the lower coupling block in the post-processing stage.

3.2 Tensor-based Degree-of-Freedom (DOF) Mapping and Mixed Boundaries

In conventional high-fidelity finite element programs, determining the mapping between local element degrees of freedom (DOFs) and global system DOFs is often one of the most time-consuming steps. This is especially true when periodic boundary conditions (PBCs) must be handled in metamaterial models. Traditional codes usually rely on multiple nested `for` loops and node-coordinate matching with geometric tolerances, so the computational cost increases with mesh resolution. To address this issue, the function `build_tensor_dof_mapping` introduces a loop-free mapping algorithm that accelerates the process using NumPy-based tensor vectorization, as illustrated in **Figure 3**.

```

33 def build_tensor_dof_mapping(voxel, dx, dy, dz, thickness):
34     nx, ny, nz = voxel.shape # Enforce XYZ indexing convention
35     node_indices = np.arange((nx + 1) * (ny + 1) * (nz + 1)).reshape(nx + 1, ny
+ 1, nz + 1)
36     dof_tensor = np.zeros((nx + 1, ny + 1, nz + 1, 3), dtype=int)
37     dof_tensor[..., 0], dof_tensor[..., 1], dof_tensor[..., 2] = node_indices *
3, node_indices * 3 + 1, node_indices * 3 + 2

```

```

38     dof_tensor[nx, :, :, :] = dof_tensor[0, :, :, :]
39     dof_tensor[:, ny, :, :] = dof_tensor[:, 0, :, :]
40
41     n1, n2 = dof_tensor[:-1, :-1, :-1, :], dof_tensor[1:, :-1, :-1, :]
42     n3, n4 = dof_tensor[1:, 1:, :-1, :], dof_tensor[:-1, 1:, :-1, :]
43     n5, n6 = dof_tensor[:-1, :-1, 1:, :], dof_tensor[1:, :-1, 1:, :]
44     n7, n8 = dof_tensor[1:, 1:, 1:, :], dof_tensor[:-1, 1:, 1:, :]
45     edof_tensor = np.concatenate([n1, n2, n3, n4, n5, n6, n7, n8], axis=-1)
46
47     active_mask = voxel > 0 # Filter out void regions
48     edofMat = edof_tensor[active_mask]
49
50     z_coords = np.linspace(dz / 2, thickness - dz / 2, nz) - thickness / 2.0
51     z_grid = np.broadcast_to(z_coords[None, None, :], (nx, ny, nz)) # Z is the
52     # 3rd axis
53     z_active = z_grid[active_mask]
54     return edofMat, z_active, node_indices.size * 3

```

This code block constructs the local-to-global DOF mapping and imposes the mixed boundary conditions required by LPS-H without introducing explicit loops.

In Lines 34-37, the nodes of the structured voxel grid are arranged regularly in space. To match the Cartesian coordinate system used in mechanics, the program adopts the indexing order x - y - z . Line 35 uses `np.arange` to generate a sequential node-index tensor for the discrete space. Line 36 then builds the four-dimensional global DOF tensor `dof_tensor` with shape $(nx+1, ny+1, nz+1, 3)$. In this tensor, the first three dimensions correspond to the 3D physical positions (x, y, z) of the nodes, while the last dimension stores the three orthogonal physical DOFs u, v , and w associated with each node.

In a traditional finite element formulation, the 2D-PBC requires the nodal displacements on opposite boundaries to be identical, namely $\mathbf{u}(L_x, y, z) = \mathbf{u}(0, y, z)$ and $\mathbf{u}(x, L_y, z) = \mathbf{u}(x, 0, z)$. These kinematic constraints are usually introduced by Lagrange multipliers or penalty methods, which increase both system size and solution complexity. By contrast, Lines 38-39 use in-place memory slicing of the global DOF tensor to overwrite the DOF numbers of the slave nodes on the $X = L_x$ and $Y = L_y$ boundaries with the corresponding master-node numbers on the negative sides. The z axis, which represents the thickness direction, is left unchanged. In this way, periodic mapping is enforced in the in-plane x and y directions while the free boundary conditions on the upper and lower surfaces are retained.

To obtain the nodal assembly relation inside each hexahedral element, Lines 41-44 use shifted array slices in different directions. For example, `[1:, :-1, :-1]` extracts the tensor `n2`, which corresponds to Node 2 after a positive shift along the x direction. Through this combination of data-structure slicing and `np.concatenate`, the DOFs of the eight corner nodes of each voxel element are extracted in a single step, and the $N_{elem} \times 24$ DOF mapping tensor `edof_tensor` for the entire computational domain is constructed. The coordinate ordering is kept consistent with the related educational paper (Andreassen and Andreasen 2014) to improve code portability.

Because metamaterials contain many topological voids, removing void elements reduces the equilibrium system and accelerates the solution. Lines 47-48 use the Boolean mask `voxel > 0` generated from the voxel model to filter out the material-free regions and obtain the compact mapping matrix `edofMat` for the active solid elements.

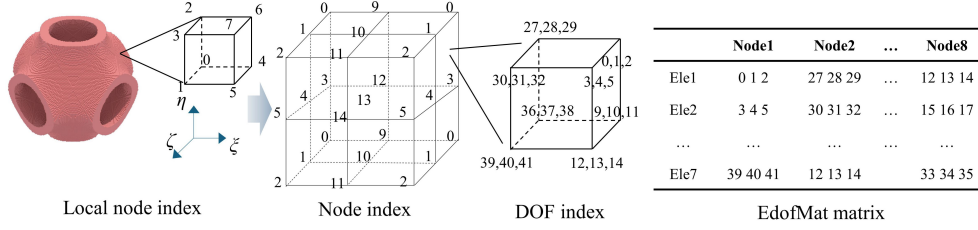


Fig. 3 Schematic of the loop-free assembly logic for the local-to-global DOF mapping tensor `edofMat` based on multidimensional tensor slicing.

Furthermore, in LPS-H, evaluation of the bending stiffness matrix \mathbf{D} and the extension-bending coupling matrix \mathbf{B} depends on the material distribution through the thickness. Lines 50-52 explicitly extract the one-dimensional vector `z_active`. Through the coordinate transformation $z = \bar{z} - h/2$, this vector computes and stores the normal thickness coordinate of the centroid of each active solid element relative to the geometric mid-surface of the macroscopic plate/shell.

3.3 Loop-Free Assembly of Global Matrices

In high-resolution voxel-based finite element analysis, assembling the global stiffness matrix \mathbf{K} and load matrix \mathbf{F} with traditional nested loops leads to substantial time overhead. To address this issue, this code block uses the low-level vectorization capability of NumPy to realize loop-free matrix assembly.

```

68     iK, jK = np.repeat(edofMat, 24, axis=1).flatten(), np.tile(edofMat, (1, 24))
        .flatten()
69     sK = np.tile(Ke.flatten(), edofMat.shape[0])
70     K = coo_matrix((sK, (iK, jK)), shape=(total_dofs, total_dofs)).tocsr() #
        Loop-free assembly of global stiffness
71
72     E_macro = np.zeros((len(z_active), 6, 6))
73     E_macro[:, 0, 0], E_macro[:, 1, 1], E_macro[:, 5, 2] = 1.0, 1.0, 1.0 #
        Apply unit membrane strains
74     E_macro[:, 0, 3], E_macro[:, 1, 4], E_macro[:, 5, 5] = z_active, z_active,
        z_active # Apply unit bending curvatures
75
76     F_ele = sum([np.einsum('ji,kjl->kil', Bs[i], np.einsum('ij,kjl->kil', C,
77     E_macro)) * detJ for i in range(8)]) # Local load via tensor contraction
        F = np.column_stack([np.bincount(edofMat.flatten(), weights=F_ele[:, :, c]).
        flatten(), minlength=total_dofs) for c in range(6)]) # Global load assembly

```

The global stiffness matrix \mathbf{K} is obtained by assembling the local element stiffness matrices \mathbf{K}_e according to the topological mapping matrix `edofMat`. The traditional approach uses `for` loops to add each 24×24 submatrix to the global matrix one by one. Lines 68-70 instead exploit the properties of the coordinate (COO) sparse matrix format to replace explicit loops with data operations. Through `np.repeat` and `np.tile`, the program tiles the local mapping tensor `edofMat` along different dimensions, thereby generating the global one-dimensional row-index vector `iK` and column-index vector `jK`, each of length $N_{active} \times 24^2$. At the same time, the element stiffness values are flattened into the one-dimensional vector `sK`. Line 70 then calls `scipy.sparse.coo_matrix`, which performs memory allocation and accumulation for

millions of nonzero entries at the underlying C level, and finally converts the result into compressed sparse row (CSR) format for better compatibility.

Before the global load vector is assembled, the six macroscopic unit deformation modes in LPS-H must be converted into local strain distributions at the microscopic scale. Line 72 initializes the three-dimensional loading super-tensor **E_macro** with shape $(N_{active}, 6, 6)$. Its first dimension corresponds to the active solid elements, its second dimension corresponds to the six components of the local strain, and its third dimension corresponds to the six independent loading cases, namely three in-plane membrane strains and three out-of-plane curvatures. In the 3D finite element formulation, the local strain vector of each microscopic solid element follows Voigt notation. Accordingly, the row indices 0 ~ 5 of **E_macro** represent

$$\boldsymbol{\varepsilon}^{3D} = [\varepsilon_{11}, \varepsilon_{22}, \varepsilon_{33}, \gamma_{23}, \gamma_{13}, \gamma_{12}]^T \quad (18)$$

In LPS-H, by contrast, six independent macroscopic deformation cases are probed in sequence. These correspond to the column indices 0 ~ 5 of **E_macro**, and the associated deformation basis vector is

$$\mathbf{E} = [\varepsilon_{11}^0, \varepsilon_{22}^0, \gamma_{12}^0, \kappa_{11}, \kappa_{22}, \kappa_{12}]^T \quad (19)$$

According to the plane-section assumption for plates, $\boldsymbol{\varepsilon} = \boldsymbol{\varepsilon}^0 + z\boldsymbol{\kappa}$. For any 3D solid element located at the normal coordinate z from the mid-surface, the initial local strain induced under the six macroscopic loading cases can be expressed explicitly through a 6×6 transformation matrix $\boldsymbol{\Gamma}(z)$:

$$\begin{aligned} \boldsymbol{\varepsilon}^{3D}(z) &= \boldsymbol{\Gamma}(z)\mathbf{I}_{6 \times 6} \\ &= \begin{matrix} & \varepsilon_{11}^0 & \varepsilon_{22}^0 & \gamma_{12}^0 & \kappa_{11} & \kappa_{22} & \kappa_{12} \\ & \downarrow & \downarrow & \downarrow & \downarrow & \downarrow & \downarrow \\ \begin{bmatrix} 1 & 0 & 0 & z & 0 & 0 \\ 0 & 1 & 0 & 0 & z & 0 \\ 0 & 0 & 0 & 0 & 0 & 0 \\ 0 & 0 & 0 & 0 & 0 & 0 \\ 0 & 0 & 0 & 0 & 0 & 0 \\ 0 & 0 & 1 & 0 & 0 & z \end{bmatrix} & \leftarrow \varepsilon_{11} \\ & \leftarrow \varepsilon_{22} \\ & \leftarrow \varepsilon_{33} \\ & \leftarrow \gamma_{23} \\ & \leftarrow \gamma_{13} \\ & \leftarrow \gamma_{12} \end{matrix} \end{matrix} \quad (20)$$

The construction of **E_macro** bridges 3D continuum mechanics and 2D plate/shell mechanics, while maintaining consistency in the application of external loading without cumbersome loops.

For Element e , under the I th deformation case, the equivalent nodal load induced by the initial macroscopic strain is written as

$$\mathbf{F}_e^{(I)} = \int_{V_e} \mathbf{B}^T \mathbf{C} \boldsymbol{\varepsilon}^{macro(I)} dV \quad (21)$$

If the traditional approach were used, evaluating this set of loads for all elements under all six loading cases would require multiple nested loops. Line 76 introduces the Einstein summation function `np.einsum`. The inner contraction, `einsum('ij,kjl->kil', C, E_macro)`, computes the initial stresses of the solid elements under the six loading cases. The outer contraction then combines these stresses

with the strain-displacement matrix $\mathbf{B}_s[i]$ at each of the eight Gauss points through loop-free tensor contraction. Because the Jacobian determinant is constant, the program multiplies directly by the integration weight $\det\mathbf{J}$ outside the contraction to obtain the local 24×6 load array \mathbf{F}_{ele} . Then, in Line 77, the one-dimensional counting function `np.bincount` is used to assemble the local load array into the six right-hand-side column vectors of the global system. Here, `bincount` treats the global DOF numbers in `edofMat` as index bins and accumulates the local nodal forces into the global load matrix \mathbf{F} using \mathbf{F}_{ele} as weights.

3.4 Asynchronous GPU Solving via CuPy

The computational bottleneck of the homogenization procedure is often the solution of the large sparse linear system $\mathbf{K}\mathbf{U} = \mathbf{F}$. To improve hardware utilization, the code uses the CuPy library to implement heterogeneous acceleration between the central processing unit (CPU) and the graphics processing unit (GPU), together with a non-blocking concurrent-stream mechanism.

```

78     active_dofs = np.setdiff1d(np.unique(edofMat), np.unique(edofMat)[:3]) #
       Eliminate rigid body motions
79
80     U = np.zeros((total_dofs, 6))
81     K_active_gpu = csp.csr_matrix(K[active_dofs, :][:, active_dofs])
82     F_active_gpu = cp.asarray(F[active_dofs, :])
83     U_active_gpu = cp.zeros((len(active_dofs), 6))
84     M_gpu = csp.diags(1.0 / K_active_gpu.diagonal())
85     streams = [cp.cuda.Stream(non_blocking=True) for _ in range(6)] #
       Initialize concurrent CUDA streams
86     for c in range(6):
87         with streams[c]: # Launch asynchronous GPU solving for 6 load cases
88             U_col_gpu, _ = cpspla.cg(K_active_gpu, F_active_gpu[:, c], M=M_gpu,
              tol=1e-6, maxiter=5000) # Jacobi Preconditioner Conjugate gradient solver
              on GPU
89             U_active_gpu[:, c] = U_col_gpu
90     for stream in streams:
91         stream.synchronize() # Barrier synchronization
92     U[active_dofs, :] = U_active_gpu.get()

```

Before solving the system, rigid-body motion must be removed. As shown in Line 78, the code uses `np.setdiff1d` to eliminate the first three DOFs as reference anchors and extract the nonsingular active DOF set `active_dofs`. In Lines 81-82, the stiffness and load matrices are converted to CuPy format and transferred to NVIDIA GPU memory. To increase the throughput of the GPU streaming multiprocessors, Line 83 instantiates six non-blocking Compute Unified Device Architecture (CUDA) streams. In the following loop, six independent Jacobi-preconditioned conjugate gradient (PCG) solves using `cpspla.cg` are dispatched to the GPU concurrently. Finally, the barrier operation `stream.synchronize()` ensures that all calculations are complete, and the results \mathbf{U} are transferred back to host memory through the `.get()` method.

The performance of this solver depends on CUDA-capable NVIDIA GPU hardware together with the CuPy heterogeneous computing library. To preserve the generality and portability of the open-source code, the original GPU solver module can be replaced by the standard sparse solver provided by SciPy when the local environment supports only CPU computation.

The CPU-only fallback code is shown below:

```

78     active_dofs = np.setdiffid(np.unique(edofMat), np.unique(edofMat)[:3]) #
       Eliminate rigid body motions
79
80     U = np.zeros((total_dofs, 6))
81     # Extract non-singular active matrices on CPU
82     K_active = K[active_dofs, :][:, active_dofs]
83     F_active = F[active_dofs, :]
84     U_active = np.zeros((len(active_dofs), 6))
85     import scipy.sparse.linalg as spla
86     for c in range(6): # Sequential solving for 6 load cases on CPU
87         U_col, _ = spla.cg(K_active, F_active[:, c]) # SciPy Conjugate gradient
            solver
88         U_active[:, c] = U_col
89     U[active_dofs, :] = U_active

```

3.5 Area Integration for ABD Matrix

After solving for the microscopic fluctuation displacement \mathbf{U} , the program recovers the physical stress field and extracts the **ABD** stiffness matrix through macroscopic area integration.

```

94     ABD = np.zeros((6, 6))
95     for i_gp in range(8):
96         Sigma = np.einsum('ij,kjl->kil', C, E_macro - np.einsum('ij,kjl->kil',
97             Bs[i_gp], U[edofMat, :])) # Recover true physical stress
98         ABD[0:3, :] += np.sum(Sigma[:, [0, 1, 5], :], axis=0) * detJ /
           plate_area # Extract A and B matrices (0th moment)
99         ABD[3:6, :] += np.sum(Sigma[:, [0, 1, 5], :] * z_active[:, None, None],
           axis=0) * detJ / plate_area # Extract D and B* matrices (1st moment)
100     return (ABD + ABD.T) / 2.0 # Symmetrization for Maxwell-Betti reciprocity

```

In a 3D heterogeneous microstructure, the local strain is the superposition of the imposed macroscopic initial strain field and the microscopic fluctuation strain caused by the pore topology. Line 96 calls the high-order tensor contraction function `np.einsum` again. By looping over `Bs[i_gp]` across the eight Gauss integration points, it recovers the microscopic stress fields of the solid elements under the six loading cases in parallel:

$$\boldsymbol{\sigma}^{(I)}(\mathbf{q}_g) = \mathbf{C} \left[\boldsymbol{\varepsilon}^{macro(I)}(z) - \mathbf{B}(\mathbf{q}_g) \mathbf{u}_e^{(I)} \right] \quad (I = 1, \dots, 6) \quad (22)$$

Here, the term $\mathbf{B}\mathbf{u}_e$ represents the relaxation effect of the microscopic fluctuation strain that arises as the structure re-establishes local equilibrium. The code directly evaluates the tensor difference `E_macro - np.einsum(...)` and multiplies it by the constitutive matrix `C`, producing the full-field stress super-tensor `Sigma` with shape $(N_{active}, 6, 6)$.

After the microscopic 3D stress field has been obtained, it must be projected onto the macroscopic internal-resultant space of the 2D plate/shell. Lines 97-98 correspond to the zeroth- and first-order spatial moment integrals of the in-plane stress resultants in LPS-H. First, the code uses the array slice `Sigma[:, [0, 1, 5], :]` to extract the in-plane stress components from the 3D stress tensor, namely $\boldsymbol{\sigma}_p = [\sigma_{11}, \sigma_{22}, \sigma_{12}]^T$. It then uses `np.sum(..., axis=0)` to perform discrete summation and integration over the volume domain of the active elements.

In Line 97, the zeroth-order stress-resultant integral is extracted. This corresponds to the extraction of the membrane stiffness matrix \mathbf{A} and the upper coupling block \mathbf{B} , where the program directly accumulates the in-plane stress over the volume and divides by the macroscopic projected area S_{plate} :

$$\mathbf{ABD}_{[0:3,:]} = \frac{1}{S_{plate}} \sum_e \sum_{g=1}^8 \sigma_p^{(I)}(\mathbf{q}_g) |J| W_g \quad (23)$$

In Line 98, the first-order stress-moment integral is extracted. This corresponds to the lower coupling block \mathbf{B}^* and the bending stiffness matrix \mathbf{D} . The program multiplies the in-plane stress by the normal thickness coordinate `z_active`, broadcast through `[:, None, None]`, to compute the first sectional moment, and again divides by the macroscopic area:

$$\mathbf{ABD}_{[3:6,:]} = \frac{1}{S_{plate}} \sum_e \sum_{g=1}^8 \sigma_p^{(I)}(\mathbf{q}_g) \cdot z_e |J| W_g \quad (24)$$

According to the Maxwell-Betti reciprocity theorem in linear elasticity, the \mathbf{ABD} stiffness matrix derived from a conservative system is theoretically symmetric, namely $\mathbf{A} = \mathbf{A}^T$, $\mathbf{D} = \mathbf{D}^T$, and the upper and lower coupling blocks satisfy $\mathbf{B} = \mathbf{B}^{*T}$. In actual numerical computation, however, the directly extracted \mathbf{ABD} matrix may exhibit slight asymmetry because of the iterative truncation tolerance of the GPU-based PCG solver and floating-point accumulation errors. To improve the rigor of the output and the stability of subsequent macroscopic finite element calls, the code performs the operation $(\mathbf{ABD} + \mathbf{ABD}.T) / 2.0$ before returning the result.

4 Examples and Discussions

4.1 Base Case Execution

4.1.1 Primitive Sandwich Lattice Structure without Skins

To demonstrate the usage logic and data flow of the open-source framework, a sheet-type Primitive structure is used below as the base case to illustrate the extraction procedure of the macroscopic effective \mathbf{ABD} stiffness matrix. The relevant results can be reproduced by running the script [examples/ex01_tpms_simulation.py](#) in the open-source repository.

First, the script defines the base-material properties and the geometric design parameters of the metamaterial plate. The base material is assigned Young’s modulus $E = 1215$ MPa and Poisson’s ratio $\nu = 0.35$. The physical thickness of the macroscopic plate/shell is set to 10 mm, the mesh resolution of the unit cell is set to $N = 96$, and the target relative density is set to 0.15, as shown in **Figure 4a**. The program then calls the function `generate_tpms_voxel_grid` from the implicit modeling module [utils/tpms_generator.py](#) to discretize a 3D voxel matrix in space using an analytical level-set equation (Ji et al. 2025):

```

1 # Step 2: Generate TPMS Voxel Model
2 from utils.tpms_generator import generate_tpms_voxel_grid

```

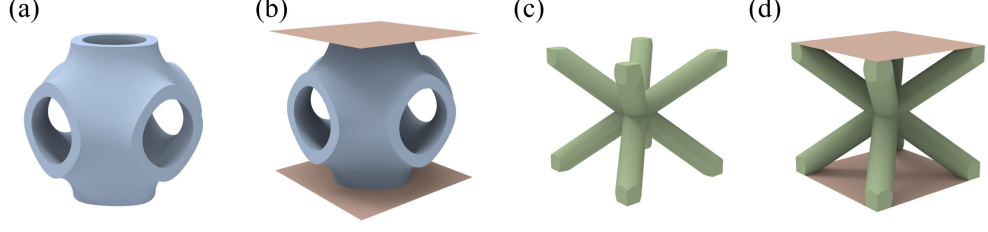


Fig. 4 Schematic illustration of the four analysis cases. (a) TPMS sandwich structure without skins. (b) TPMS sandwich structure with skins. (c) BCC sandwich structure without skins. (d) BCC sandwich structure with skins.

```

3 voxel_grid = generate_tpms_voxel_grid(
4     tpms_type='Primitive',
5     Nx=1, Ny=1, Nz=1,
6     resolution=96,
7     relative_density=0.15, # Volume fraction
8     is_sheet=True
9 )

```

The generated `voxel_grid` is then passed, together with the physical parameters, to the heterogeneous solver `homogenization_plate` developed in Section 2.

```

1 # Step 3: Execute GPU-Accelerated LPS-H
2 ABD_matrix = homogenization_plate(
3     voxel=voxel_grid,
4     E=E_base,
5     nu=nu_base,
6     thickness=thickness,
7     Nx=Nx, Ny=Ny, Nz=Nz
8 )

```

The entire solution takes 28.40 s and yields the following 6×6 macroscopic effective stiffness matrix for the equivalent continuum:

$$\mathbf{ABD}_{Primitive} = \begin{bmatrix} 356.12 & 202.24 & 0.00 & \vdots & -0.09 & -0.01 & -0.04 \\ 202.24 & 356.12 & 0.00 & \vdots & -0.04 & -0.04 & -0.04 \\ 0.00 & 0.00 & 308.85 & \vdots & -0.04 & -0.04 & -0.06 \\ \dots & \dots & \dots & \dots & \dots & \dots & \dots \\ -0.09 & -0.04 & -0.04 & \vdots & 2229.51 & 1455.26 & 0.01 \\ -0.01 & -0.04 & -0.04 & \vdots & 1455.26 & 2229.43 & 0.04 \\ -0.04 & -0.04 & -0.06 & \vdots & 0.01 & 0.04 & 2024.48 \end{bmatrix} \quad (25)$$

Quantitatively, for the in-plane membrane stiffness matrix \mathbf{A} , the diagonal entries A_{11} and A_{22} are nearly identical at 356.12 MPa·mm, and the in-plane extension-shear coupling terms A_{16} and A_{26} are close to zero. This indicates that the Primitive structure is orthotropic in the macroscopic x - y plane. For the extension-bending coupling

matrix \mathbf{B} , most B_{ij} values are on the order of 10^{-2} and can be regarded as numerical truncation error. Numerically, this indicates that the constructed sheet-type Primitive unit cell is approximately symmetric about the macroscopic geometric mid-surface, so in-plane deformation and out-of-plane bending are nearly decoupled. For the bending stiffness matrix \mathbf{D} , the values of D_{11} and D_{22} are also close, at about 2229.5 MPa·mm³, and the bending-twist coupling terms D_{16} and D_{26} are likewise close to zero. This suggests that parasitic geometric twisting is weak when the metamaterial plate is subjected to pure bending moments, which is characteristic of an orthotropic thin plate in bending.

4.1.2 Primitive Sandwich Lattice Structure with Skins

In practical engineering applications, Lattice-skin Plate Structures usually appear as sandwich structures composed of a lattice core and dense skins. Compared with a single lattice topology, the introduction of skins can protect the core cells from environmental exposure and improve the out-of-plane bending resistance of the plate/shell. The following example shows a typical workflow for analyzing a Lattice-skin Plate Structure with this framework. By adding a NumPy padding operation after the voxel-generation block of `ex01_tpms_simulation.py`, a skinned model can be created:

```

1     voxel_grid = np.pad(
2         voxel_grid,
3         pad_width=((0, 0), (0, 0), (2, 2)),
4         mode='constant',
5         constant_values=1
6     )

```

For the sheet-type Primitive structure with added skins, the relative density and thickness are kept at 0.15 and 10 mm, respectively. The model is shown in **Figure 4b**. The program outputs the following effective **ABD** stiffness matrix:

$$\mathbf{ABD}_{Skinned} = \begin{bmatrix}
 973.08 & 412.50 & 0.00 & \vdots & -0.08 & -0.06 & -0.03 \\
 412.50 & 973.08 & 0.00 & \vdots & -0.06 & -0.08 & -0.03 \\
 0.00 & 0.00 & 512.03 & \vdots & -0.04 & -0.04 & -0.07 \\
 \dots & \dots & \dots & \dots & \dots & \dots & \dots \\
 -0.08 & -0.06 & -0.04 & \vdots & 16538.85 & 6436.16 & 0.03 \\
 -0.06 & -0.08 & -0.04 & \vdots & 6436.16 & 16538.85 & 0.03 \\
 -0.03 & -0.03 & -0.07 & \vdots & 0.03 & 0.03 & 6543.43
 \end{bmatrix} \quad (26)$$

The results give $A_{11} = A_{22} = 973.08$ MPa·mm and $D_{11} = D_{22} = 16538.85$ MPa·mm³. The addition of skins increases the in-plane membrane stiffness by about 170%, while the bending stiffness D_{11} rises from about 2229 to 16538, an increase of about 640%. This indicates that Lattice-skin Plate Structures can provide higher stiffness in applications, such as aerospace, where bending resistance is important.

4.1.3 BCC Sandwich Lattice Structure without Skins

To further verify the generality and numerical stability of the open-source framework for truss-based structures, a classical body-centered cubic (BCC) lattice is selected as a validation case. The results can be reproduced by running the script [examples/ex01_2_lattice_simulation.py](#) in the open-source repository. The same physical parameters as in the TPMS case are used: $E = 1215$ MPa, $\nu = 0.35$, thickness 10 mm, and target relative density 0.15. The model is shown in **Figure 4c**. The effective **ABD** stiffness matrix of the structure without skins is then obtained through the implicit truss modeling module [utils/lattice_generator.py](#):

$$\mathbf{ABD}_{BCC} = \begin{bmatrix} 68.84 & 32.12 & -0.07 & \vdots & 0.21 & -0.19 & 0.18 \\ 32.12 & 68.84 & -0.01 & \vdots & -0.16 & 0.18 & 0.19 \\ -0.07 & -0.01 & 256.47 & \vdots & 0.20 & 0.16 & 0.82 \\ \dots & \dots & \dots & \dots & \dots & \dots & \dots \\ 0.21 & -0.16 & 0.20 & \vdots & 625.52 & 234.58 & -0.31 \\ -0.19 & 0.18 & 0.16 & \vdots & 234.58 & 625.55 & 0.17 \\ 0.18 & 0.19 & 0.82 & \vdots & -0.31 & 0.17 & 1674.86 \end{bmatrix} \quad (27)$$

This matrix shows that the BCC lattice structure also exhibits orthotropic behavior in its macroscopic mechanical response. Its in-plane membrane stiffnesses A_{11} and A_{22} are both 68.84 MPa·mm, and the extension-shear coupling terms are close to zero. Compared with the pure tensile stiffness, the in-plane shear stiffness A_{66} of the BCC structure is 256.47 MPa·mm, which is larger than A_{11} . This is closely related to its topology of spatial diagonal struts: the BCC topology is bending-dominated under principal-axis tension/compression, but becomes stretch-dominated under shear. In addition, the entries of the extension-bending coupling block **B** remain within a small numerical truncation range, indicating macroscopic geometric mid-surface symmetry. For bending resistance, D_{11} and D_{22} are close to each other, at about 625.5 MPa·mm³, and the bending-twist coupling terms also approach zero, which is consistent with the bending behavior of an orthotropic thin plate.

4.1.4 BCC Sandwich Lattice Structure with Skins

Similarly, to investigate the mechanical enhancement effect of dense skins on a discrete lattice architecture, top and bottom NumPy padding layers are added to the BCC unit-cell model above, and the homogenization analysis is repeated. The model is shown in **Figure 4d**. The resulting macroscopic effective **ABD** stiffness matrix of the skinned BCC sandwich plate is

$$\mathbf{ABD}_{BCC_Skinned} = \begin{bmatrix} 667.89 & 241.00 & -0.08 & \vdots & 1.20 & 0.18 & 0.18 \\ 241.00 & 667.78 & -0.05 & \vdots & 0.22 & 0.89 & 0.23 \\ -0.08 & -0.05 & 437.42 & \vdots & 0.19 & 0.19 & 0.80 \\ \dots & \dots & \dots & \dots & \dots & \dots & \dots \\ 1.20 & 0.22 & 0.19 & \vdots & 14513.15 & 5072.29 & -0.41 \\ 0.18 & 0.89 & 0.19 & \vdots & 5072.29 & 14511.40 & -0.26 \\ 0.18 & 0.23 & 0.80 & \vdots & -0.41 & -0.26 & 5921.17 \end{bmatrix} \quad (28)$$

Compared with the pure BCC lattice structure without skins, the introduction of skins increases the overall effective stiffness. The in-plane principal stiffness A_{11} increases from 68.84 MPa·mm to 667.89 MPa·mm, an increase of about 870%. The bending stiffness D_{11} increases from 625.52 MPa·mm³ to 14513.15 MPa·mm³, an increase of about 2200%. This indicates that skins located far from the neutral surface improve the bending efficiency of the section and dominate when the thin-walled plate/shell carries out-of-plane bending moments. Together with the TPMS examples above, these results show that the framework has good applicability and stability in cross-dimensional stiffness tensor assembly. They also indicate that LPS-H can be used for metamaterial laminated structures with multiscale geometric features, providing an analysis tool for the development and design of multifunctional lightweight Lattice-skin Plate Structures.

4.2 Mesh Convergence Analysis

In voxel-based finite element homogenization, the mesh resolution affects both the geometric fidelity of the implicit surface boundary and the number of DOFs in the discrete model. To balance computational accuracy and efficiency, a mesh convergence analysis is carried out for the LPS-H framework. The sheet-type Primitive structure is selected as the reference case, while the cell array and the relative density of 0.15 are kept unchanged. The one-dimensional mesh resolution of the unit cell, N , is increased from 20 to 125 with a sampling interval of 5. The in-plane principal tensile stiffness A_{11} and the out-of-plane principal bending stiffness D_{11} are extracted from the effective stiffness matrix at each resolution. Their convergence histories are shown in **Figure 5**.

The results show that when the one-dimensional mesh resolution is low, the predicted in-plane and out-of-plane stiffness values exhibit noticeable fluctuations. This is related to the stair-step modeling effect produced when a coarse voxel grid approximates a complex TPMS surface. As the mesh resolution increases, the voxel model approximates the implicit surface more accurately and the stair-step effect gradually weakens. When N exceeds 60, the values of A_{11} and D_{11} become stable and show asymptotic convergence.

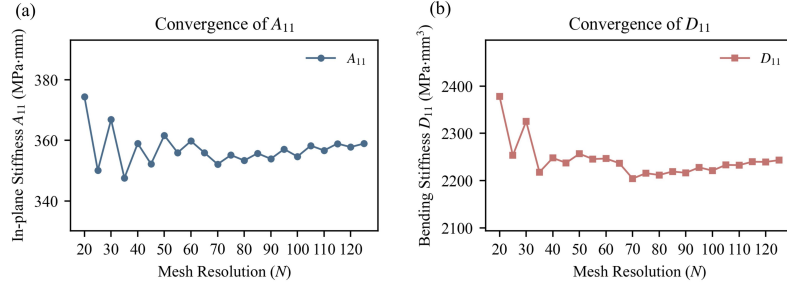


Fig. 5 Mesh convergence analysis of the sheet-type Primitive structure. (a) Evolution of the in-plane membrane stiffness A_{11} with respect to the resolution N . (b) Evolution of the bending stiffness D_{11} with respect to the resolution N .

Further increasing the resolution can improve the approximation of the analytical geometry, but the total number of DOFs in 3D voxel-based finite elements is proportional to N^3 , so the memory cost and solution time also increase. Based on the convergence analysis and the numerical stability discussion above, a unit-cell mesh resolution in the range $N = 60 \sim 65$ is a reasonable choice for LPS-H performance evaluation of thin-walled TPMS plate/shells. This range balances mechanical accuracy and GPU-based solution efficiency, and can be used as a practical compromise in engineering analysis.

4.3 Anisotropy and Extension-Twist Coupling in TPMS Plates

A benchmark comparison between LVS-H and LPS-H is presented below. The analysis considers four representative sheet-type TPMS structures, namely Gyroid, Diamond, Primitive, and I-WP. Both homogenization methods use a mesh resolution of 128^3 , a relative density of 0.15, and a physical thickness of 10 mm. Only a single truncated period is retained through the thickness, i.e., $N_z = 1$. Heat maps comparing the effective **ABD** stiffness matrices extracted by LPS-H with the predictions from LVS-H, together with the corresponding relative-error distributions, are shown in **Figure 6**. The results indicate that LVS-H exhibits bias in both stiffness prediction and coupling-response characterization for finite-thickness structures.

Because LVS-H imposes 3D-PBC in all three spatial directions, the equivalent model tends to preserve the symmetry of the spatial lattice. As a result, LVS-H predicts identical in-plane tensile stiffness for the Gyroid structure, namely $A_{11} = A_{22} = 674.00$ MPa-mm. When the continuous Gyroid surface is physically truncated into a single-layer thin plate with thickness 10 mm, however, the asymmetric truncation of the upper and lower surfaces breaks the original body-centered cubic symmetry and induces macroscopic in-plane orthotropy. The LPS-H results show a clear stiffness difference, with $A_{11} = 448.68$ MPa-mm and $A_{22} = 627.66$ MPa-mm. Relative to the LPS-H results, the LVS-H predictions of tensile stiffness are higher by 50.22% and 7.49% in the x and y directions, respectively.

LVS-H also overestimates the out-of-plane bending stiffness matrix **D**. The bending-stiffness prediction errors for the four structures are 151.09%, 15.35%, 221.11%, and 37.24%, respectively. This indicates that LVS-H mathematically assumes

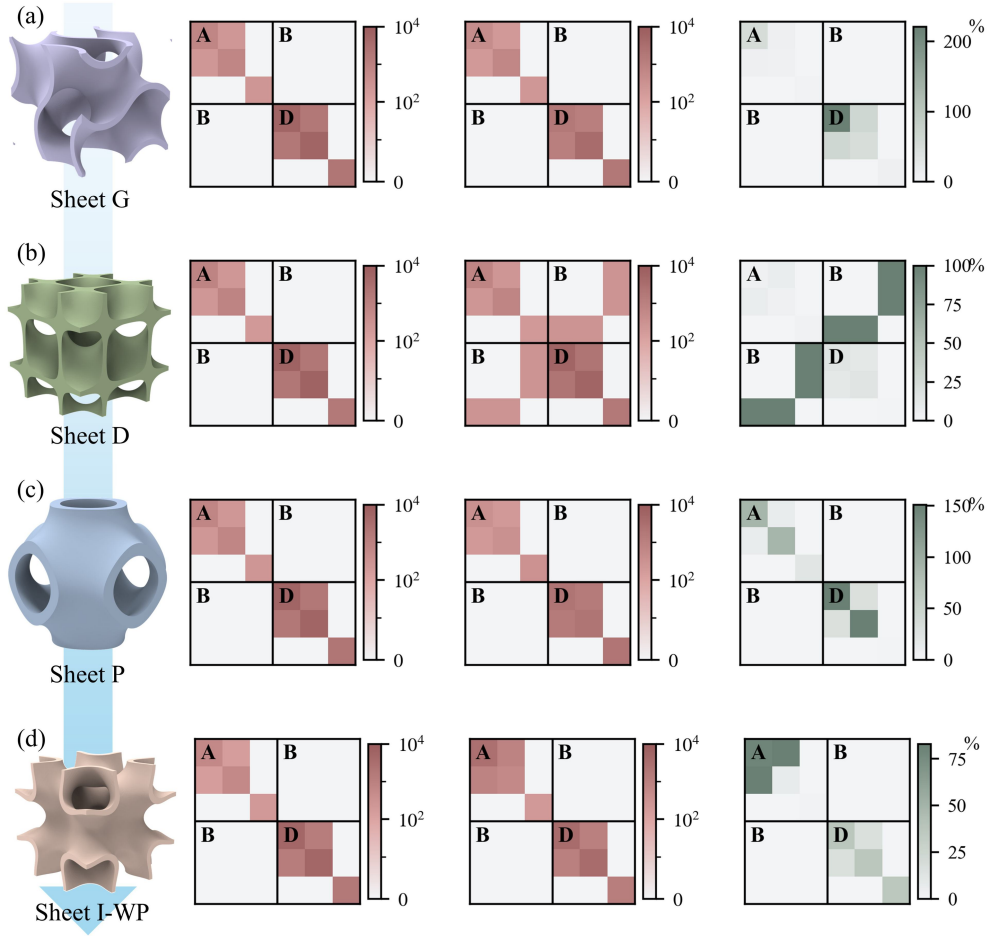


Fig. 6 Heat-map comparison of effective **ABD** stiffness predictions from LVS-H and LPS-H for sheet-type TPMS structures, together with the corresponding relative-error distributions.

a uniform material distribution through the thickness direction z , which changes the sectional moment of inertia of the structure.

In addition, the three-dimensional periodic boundaries used in LVS-H cannot fully reflect the intrinsic asymmetric coupling deformation mechanisms of the topology. Taking the sheet-type Diamond structure as an example, the LPS-H results show nonzero terms B_{16} and B_{26} in the extension-bending coupling matrix, with values reaching $285.07 \text{ MPa}\cdot\text{mm}^2$. These nonzero terms indicate a macroscopic extension-twist coupling effect. Under in-plane uniaxial tension, the plate/shell may therefore undergo macroscopic out-of-plane twisting deformation.

4.4 Thickness Size Effect and Asymptotic Convergence

In classical continuum mechanics, as the plate/shell thickness increases, the influence of surface boundary conditions on macroscopic stiffness gradually decays, and finite-thickness plate theory asymptotically approaches 3D solid theory. To evaluate the physical consistency and generality of the open-source code, the thickness size effect of metamaterial plates is analyzed below. The results can be reproduced by running [examples/ex02_multiple_cells.py](#). Taking the sheet-type Gyroid structure as an example, the in-plane cell count is kept at 1×1 , while the number of cells through the thickness, N_z , is increased from 1 to 12, as shown in **Figure 7(a)**. For convenience of comparison, each stiffness component computed by LPS-H is normalized by the theoretical stiffness value derived from LVS-H together with the corresponding formulas. The convergence curves of the normalized in-plane membrane stiffness A_{ij} and out-of-plane bending stiffness D_{ij} versus the layer number N_z are shown in **Figure 7(b)** and **(c)**, respectively. The dashed line at 1.0 represents the LVS-H prediction benchmark.

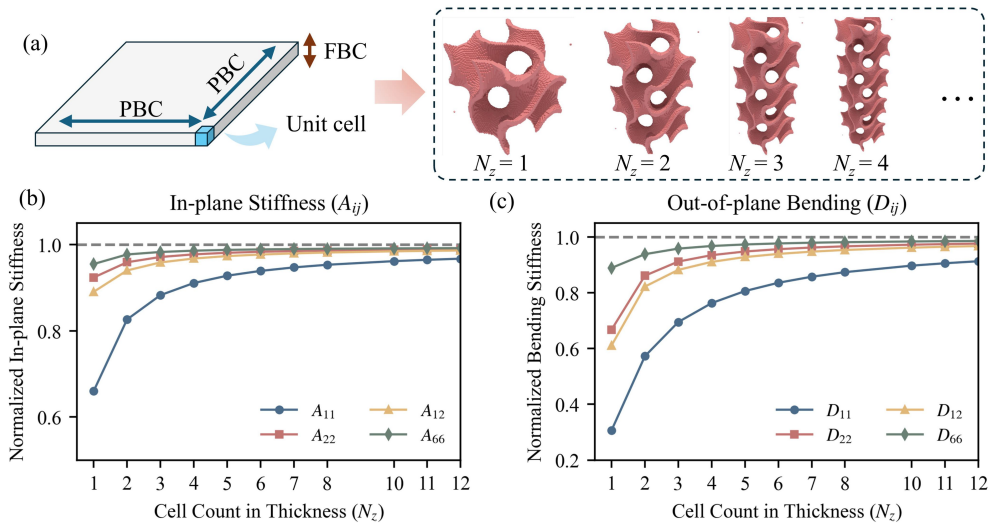


Fig. 7 Thickness size-effect analysis of the sheet-type Gyroid structure. (a) Schematic of the geometric evolution as the number of layers through the thickness, N_z , increases; in-plane periodic boundary conditions (PBC) are applied and out-of-plane free boundary conditions (FBC) are retained. (b) Convergence curves of the normalized in-plane membrane stiffness A_{ij} versus N_z . (c) Convergence curves of the normalized bending stiffness D_{ij} versus N_z .

The results show that when the number of layers is small, the predictions of LPS-H and LVS-H differ substantially. For the thin plate with $N_z = 1$, the normalized in-plane principal stiffnesses A_{11} and A_{22} are 0.66 and 0.92, respectively. Relative to the LPS-H results, the corresponding LVS-H predictions are higher by 51.5% and 8.7%. The discrepancy is even more pronounced for the bending stiffness, where the normalized values of D_{11} and D_{22} are 0.31 and 0.67, corresponding to deviations

of 226.3% and 49.7%. As the number of layers through the thickness increases, the normalized stiffness curves increase monotonically and gradually approach 1.0. For the in-plane stiffness, the normalized values exceed 0.90 and 0.95 at 4 and 8 layers, respectively. For the out-of-plane stiffness, the normalized values exceed 0.90 when the number of layers reaches 11.

5 Extensions

5.1 Extension to Multimaterial Lattice-skin Plate Structures

With the development of additive manufacturing, metamaterial plate/shells printed from multiple base materials are becoming a new paradigm in structural design. In multimaterial systems, the constitutive relation is no longer a global constant. Instead, it becomes a nonuniform tensor field $\mathbf{C}(\mathbf{x})$ that varies with spatial position. The following shows how the single-phase LPS-H framework can be extended to multimaterial homogenization with only modest code modifications.

From both the physical and mathematical viewpoints, the main change introduced by multiple materials is that each discrete voxel element e has its own local material properties, such as Young’s modulus E_e and Poisson’s ratio ν_e . Accordingly, the integral formula for the element stiffness matrix must be modified to depend on the local constitutive tensor \mathbf{C}_e :

$$\mathbf{K}_e^{(e)} = \int_{V_e} \mathbf{B}^T \mathbf{C}_e \mathbf{B} dV = \sum_{g=1}^8 \mathbf{B}^T(\mathbf{q}_g) \mathbf{C}_e \mathbf{B}(\mathbf{q}_g) |J| W_g \quad (29)$$

In the Python implementation, preserving the loop-free computational efficiency of the framework requires abandoning the traditional element-by-element traversal used in finite element codes and continuing to exploit the advantages of NumPy multidimensional tensor operations. The main modifications are concentrated in the following three modules:

Initialization of the material constitutive tensor field

In the original code, \mathbf{C} is a two-dimensional array with shape 6×6 . For multimaterial analysis, a three-dimensional super-tensor `C_active` with shape $(N_{active}, 6, 6)$ must be generated for the active elements according to the spatial position or phase state of the voxels. In practical metamaterial engineering, two multimaterial-definition scenarios are common:

Scenario A: regular partition based on spatial coordinates

Consider a typical bimaterial laminated plate, as shown in **Figure 8**, in which the base material has Young’s modulus 500 MPa in the upper half through the thickness, $z > 0$, and 1215 MPa in the lower half, $z \leq 0$. A vectorized initialization can be performed using the conditional-selection functionality of NumPy based on the thickness coordinates `z_active` of the elements.

Scenario B: arbitrary irregular phase mapping based on a voxel matrix

More generally, the material distribution inside many multimaterial structures is irregular. In this case, an external material-label matrix `material_grid`, consistent with

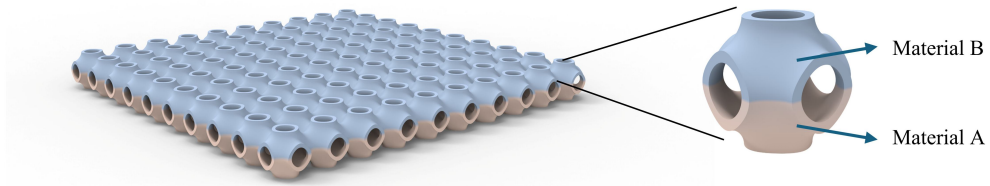


Fig. 8 Schematic of a bimaterial laminated metamaterial plate/shell.

the structural geometry and of size $N_x \times N_y \times N_z$, is usually maintained. Here, the value 1 represents the first material, 2 represents the second material, and so on. In the code, Boolean masking can be used to extract the material IDs of the active elements, and `np.select` can then realize loop-free mapping of multiphase material properties.

Efficient vectorized implementations of these two scenarios in Python are shown below:

```

1  # =====
2  # Scenario A: Based on spatial coordinates (e.g., Bi-material plate)
3  # =====
4  E_active = np.where(z_active > 0, 500.0, 1215.0)
5
6  # =====
7  # Scenario B: Based on an explicit material matrix (e.g., Custom field)
8  # =====
9  # Assume 'material_grid' is passed into the function alongside 'voxel'
10 # Extract material IDs exclusively for the solid active elements
11 # mat_id_active = material_grid[active_mask]
12
13 # Map material IDs to real physical parameters without any loops
14 conditions = [mat_id_active == 1, mat_id_active == 2]
15 choices = [1215.0, 500.0] # E.g., Material 1 is 1215 MPa, Material 2 is 500
    MPa
16
17 # Assign default modulus (e.g., 10.0 MPa) to any unmapped IDs as a fallback
18 E_active = np.select(conditions, choices, default=10.0)
19
20 # Finally, build the heterogenous constitutive super-tensor
21 # 'get_multi_material_elasticity' handles the array of E efficiently
22 C_active = get_multi_material_elasticity(E_active, nu_base) # Shape: (
    N_active, 6, 6)

```

At the same time, a new function, `get_multi_material_elasticity`, is introduced to replace the original `get_isotropic_elasticity` function.

```

1  def get_multi_material_elasticity(E_array, nu=0.3):
2      lam = E_array * nu / ((1 + nu) * (1 - 2 * nu))
3      mu = E_array / (2 * (1 + nu))
4      N = len(E_array)
5      C_active = np.zeros((N, 6, 6))
6      C_active[:, 0, 1] = C_active[:, 0, 2] = C_active[:, 1, 0] = lam

```

```

7     C_active[:, 1, 2] = C_active[:, 2, 0] = C_active[:, 2, 1] = lam
8     C_active[:, 0, 0] = C_active[:, 1, 1] = C_active[:, 2, 2] = lam + 2 * mu
9     C_active[:, 3, 3] = C_active[:, 4, 4] = C_active[:, 5, 5] = mu
10    return C_active

```

Vectorized assembly of heterogeneous element stiffness and loads

Because the constitutive tensor \mathbf{C}_e differs from one element to another, the original operation `np.tile`, which replicates a single \mathbf{K}_e , is no longer applicable. Instead, higher-order tensor contraction must be used to compute the individual stiffness matrices of all active elements simultaneously. The original assembly logic can be replaced by the following `np.einsum`-based operations:

```

1     # Compute active element stiffness matrices simultaneously
2     Ke_active = np.zeros((len(edofMat), 24, 24))
3     for i in range(8):
4         # np.einsum notation: 'ji' (B.T), 'ekj' (C_active), 'kl' (B) -> 'eil' (
5         #   Ke for each element e)
6         Ke_active += np.einsum('ji,ekj,kl->eil', Bs[i], C_active, Bs[i]) * detJ
7
8     # Flatten the heterogeneous stiffness array directly for COO matrix
9     sK = Ke_active.flatten()

```

For the calculation of the initial macroscopic loads, the original broadcast multiplication must likewise be upgraded to a contraction that accounts for the element dimension:

```

1     # Modify local load calculation for multi-material
2     F_ele = sum([np.einsum('ji,ejl->eil', Bs[i],
3         np.einsum('eij,ejl->eil', C_active, E_macro)) * detJ for i in
4         range(8)])

```

Here, `eij,ejl->eil` specifies one-to-one multiplication of tensors along the first dimension `e`, where `e` is the element index, thereby realizing the physical mapping of material heterogeneity.

Heterogeneous stress recovery

Similarly, during the final macroscopic area-integration stage for extracting the **ABD** matrix, recovery of the physical stress $\mathbf{\Sigma}$ must also depend on the local `C_active`. The stress calculation in Line 96 of the original code should therefore be modified as follows:

```

1     # Recover true physical stress utilizing local constitutive tensors
2     Sigma = np.einsum('eij,ejl->eil', C_active,
3         E_macro - np.einsum('ij,ejl->eil', Bs[i_gp], U[edofMat,
4         :]))

```

By introducing the dimension `'e'` into the `einsum` string specification above, LPS-H analysis can be extended to multimaterial, multiphase, and even damage-containing materials defined by arbitrary voxels, without increasing the nesting depth of Python `for` loops.

Running the script `examples/ex03_multimaterial_simulation.py` in the open-source repository produces the following 6×6 macroscopic effective stiffness matrix for the bimaterial case:

$$\mathbf{ABD}_{Bi-material} = \begin{bmatrix} 245.86 & 147.49 & 0.00 & \vdots & -229.85 & -176.77 & -0.02 \\ 147.49 & 245.86 & 0.00 & \vdots & -176.77 & -229.85 & -0.02 \\ 0.00 & 0.00 & 217.04 & \vdots & -0.02 & -0.02 & -223.64 \\ \dots & \dots & \dots & \dots & \dots & \dots & \dots \\ -229.85 & -176.77 & -0.02 & \vdots & 1564.58 & 1033.34 & 0.03 \\ -176.77 & -229.85 & -0.02 & \vdots & 1033.34 & 1564.58 & 0.03 \\ -0.02 & -0.02 & -223.64 & \vdots & 0.03 & 0.03 & 1417.09 \end{bmatrix} \quad (30)$$

Compared with the \mathbf{ABD} matrix of the single-phase homogeneous material in Section 4, the \mathbf{B} matrix entries of the multimaterial structure are no longer zero. The main terms, such as B_{11} and B_{12} , are -229.85 and -176.77 MPa \cdot mm², respectively. This indicates that when pure in-plane tension is applied to the bimaterial metamaterial plate/shell, macroscopic bending deformation may occur because of stress mismatch between the upper and lower layers.

5.2 Extension to Thermal Conduction Homogenization

With the continuing miniaturization and increasing power density of aerospace electronic devices, metamaterial plate/shells capable of integrating structural and thermal functions have become of interest for thermal protection and heat-dissipation design. In continuum mechanics, the weak forms of the linear elastic static equations and the steady-state heat conduction equations are highly isomorphic. The following shows how this similarity can be used to extend the LPS-H mechanical code into a tool for predicting effective in-plane thermal conductivity.

In steady-state heat conduction theory, the basic mapping of physical variables is as follows: the displacement vector \mathbf{u} is replaced by the temperature field T ; the strain tensor $\boldsymbol{\varepsilon}$ maps to the temperature gradient ∇T ; the stress tensor $\boldsymbol{\sigma}$ maps to the heat-flux vector \mathbf{q} ; and the elastic constitutive matrix \mathbf{C} corresponds to the thermal conductivity tensor \mathbf{k} . Fourier's law of heat conduction can be written as $\mathbf{q} = -\mathbf{k}\nabla T$.

Scalar reduction of the global DOF field

In the mechanical analysis, each node has three translational DOFs, namely (u, v, w) . In the heat-conduction problem, however, each node has only one scalar DOF, namely the temperature T . Therefore, the tensorized DOF mapping function `build_tensor_dof_mapping` must be modified for the global DOF tensor `dof_tensor`:

```

1   # Thermal DOF mapping: 1 Degree of Freedom (Temperature) per node
2   node_indices = np.arange((nx + 1) * (ny + 1) * (nz + 1)).reshape(nx + 1, ny
3   + 1, nz + 1)
4   dof_tensor = node_indices.copy() # No need for the last axis of length 3
5
6   # 2D-PBC bounds apply exactly as before
7   dof_tensor[nx, :, :] = dof_tensor[0, :, :]

```

```
7 dof_tensor[:, ny, :] = dof_tensor[:, 0, :]
```

Vectorized construction of the element thermal conduction matrix and loads

For an isotropic base material, the thermal conductivity tensor is the diagonal matrix $\mathbf{k} = k_{base}\mathbf{I}_{3\times 3}$. The element-level conduction matrix becomes

$$\mathbf{K}_T^{(e)} = \int_{V_e} (\nabla\mathbf{N})^T \mathbf{k} (\nabla\mathbf{N}) dV \quad (31)$$

Because the temperature field is a scalar field, the original strain-displacement matrix \mathbf{B} of size 6×24 must be replaced by the 3×8 shape-function gradient matrix $\nabla\mathbf{N}$. In the original code, the derivative assembly is therefore simplified to the matrix $d\mathbf{N}$:

```
1 # Element Thermal Conductivity Matrix
2 Kt_e, gradNs = np.zeros((8, 8)), []
3 for q in nodes / np.sqrt(3):
4     # dN is the 3x8 gradient matrix of shape functions
5     dN = 0.125 * np.array([(1 + q[1] * nodes[:, 1]) * (1 + q[2] * nodes[:,
6     2]) * nodes[:, 0] * (2 / dx), (1 + q[0] * nodes[:, 0]) * (1 + q[2] * nodes
7    [:, 2]) * nodes[:, 1] * (2 / dy), (1 + q[0] * nodes[:, 0]) * (1 + q[1] *
8     nodes[:, 1]) * nodes[:, 2] * (2 / dz)])
9     gradNs.append(dN)
10    Kt_e += dN.T @ k_tensor @ dN * detJ
```

Macroscopic temperature-gradient loading and extraction of effective thermal conductivity

For the 2D dimension-reduced heat-transfer analysis of a sheet-type plate/shell, the quantity of interest is the in-plane heat-dissipation efficiency. Therefore, only two macroscopic unit temperature-gradient cases need to be applied, namely the temperature gradients along the x and y axes, $\nabla T_{macro} = [1, 0, 0]^T$ and $[0, 1, 0]^T$. The macroscopic excitation tensor $\mathbf{Grad_macro}$ thus becomes a matrix with shape $(3, 2)$.

After the same PCG-based heterogeneous solver is used to obtain the microscopic temperature fluctuation field \mathbf{T}_{fluc} , the macroscopic effective thermal conductivity matrix \mathbf{k}^{hom} can be extracted by integrating the in-plane heat-flux density. Here, \mathbf{T}_{fluc} has shape $N_{dofs} \times 2$, while \mathbf{k}^{hom} has size 2×2 :

```
1 k_hom = np.zeros((2, 2))
2 for i_gp in range(8):
3     # Recover True Heat Flux (q = k * (Grad_macro + gradN * T_fluc))
4     Flux = np.einsum('ij, j1->i1', k_tensor, Grad_macro - np.einsum('ij, ej1
5     ->e11', gradNs[i_gp], T_fluc[edofMat, :]))
6
7     # Extract 2x2 in-plane thermal conductivity matrix via area integration
8     k_hom += np.sum(Flux[:, 0:2, :], axis=0) * detJ / plate_area
```

Running the script [examples/ex04_tpms_thermal_simulation.py](#) in the open-source repository produces the following 2×2 macroscopic effective in-plane thermal conductivity matrix:

$$\mathbf{k}^{hom} = \begin{bmatrix} 60.19 & 0.00 \\ 0.00 & 60.19 \end{bmatrix} \quad (32)$$

The above calculation results are based on the following standard test parameters: the analysis object is the sheet-type Primitive structure, the unit-cell relative density is $\bar{\rho} = 0.15$, the overall plate thickness is $h = 10$ mm, and the homogeneous base material is assigned a thermal conductivity of $k_s = 60.5$ W/(m · K).

6 Conclusion

For the dimensional-reduction analysis of Lattice-skin Plate Structures, the open-source Python implementation of LPS-H alleviates the limitations of LVS-H in the analysis of finite-thickness thin-walled structures. Because LVS-H is constrained by the periodic assumption through the thickness, it may overestimate out-of-plane bending stiffness and neglect the extension-bending and extension-twist coupling effects caused by surface truncation when finite-thickness thin-walled structures are analyzed. The proposed computational framework introduces mixed boundary conditions that are periodic in plane and free out of plane. These boundary conditions help reflect the underlying mechanical mechanisms and enable reduced-order extraction of the macroscopic effective **ABD** stiffness matrix.

At the algorithmic level, the program replaces the conventional element-by-element nested assembly loops in finite element analysis with a loop-free topological DOF mapping algorithm based on multidimensional array slicing, together with high-order tensor contraction using `np.einsum`. These techniques enable vectorized assembly of the global stiffness and load matrices. Combined with the non-blocking CUDA-stream concurrency mechanism provided by CuPy and the Jacobi-preconditioned conjugate gradient solver, the heterogeneous acceleration framework can solve high-fidelity metamaterial unit-cell models containing millions of DOFs.

The benchmark tests and convergence analyses show that complex metamaterial plate/shells exhibit thickness size effects and macroscopic anisotropy. The results further verify the numerical stability and theoretical consistency of the algorithm across different mesh resolutions. Owing to its generalized vectorized programming architecture, the homogenization code can be extended to the analysis of multiphase laminated structures and to multiphysics performance evaluation such as steady-state heat conduction. The open-source code provided here can serve as a foundational analysis tool for computational mechanics education and for the high-fidelity structural design and topology optimization of multifunctional thin-walled metamaterials.

Appendix A A 99-line Python Code for ABD Matrix Homogenization

```

1 import numpy as np
2 from scipy.sparse import coo_matrix
3 import cupy as cp
4 import cupyx.scipy.sparse as csp

```

```

5 import cupyx.scipy.sparse.linalg as cpspla
6
7
8 def get_isotropic_elasticity(E=1.0, nu=0.3):
9     lam, mu = E * nu / ((1 + nu) * (1 - 2 * nu)), E / (2 * (1 +
10         nu)) # Calculate Lamé parameters
11     C = np.zeros((6, 6)) # Initialize 6x6 constitutive matrix
12     C[0:3, 0:3] = lam
13     np.fill_diagonal(C[0:3, 0:3], lam + 2 * mu)
14     np.fill_diagonal(C[3:6, 3:6], mu)
15     return C
16
17 def compute_element_stiffness(C, dx, dy, dz):
18     Ke, Bs = np.zeros((24, 24)), []
19     nodes = np.array([[ -1, -1, -1], [ 1, -1, -1], [ 1, 1, -1],
20         [-1, 1, -1], [-1, -1, 1], [ 1, -1, 1], [ 1, 1, 1], [-1, 1,
21         1]]) # 8-node local coordinates
22     detJ = dx * dy * dz / 8.0
23     for q in nodes / np.sqrt(3): # Loop over 8 Gauss
24         # integration points
25         dN = 0.125 * np.array([(1 + q[1] * nodes[:, 1]) * (1 +
26             q[2] * nodes[:, 2]) * nodes[:, 0] * (2 / dx), (1 + q[0] *
27             nodes[:, 0]) * (1 + q[2] * nodes[:, 2]) * nodes[:, 1] * (2
28             / dy), (1 + q[0] * nodes[:, 0]) * (1 + q[1] * nodes[:, 1])
29             * nodes[:, 2] * (2 / dz)]) # Cartesian derivatives
30         B = np.zeros((6, 24)) # Strain-displacement matrix
31         B[0, 0::3], B[1, 1::3], B[2, 2::3] = dN[0], dN[1], dN
32         [2]
33         B[3, 1::3], B[3, 2::3] = dN[2], dN[1]
34         B[4, 0::3], B[4, 2::3] = dN[2], dN[0]
35         B[5, 0::3], B[5, 1::3] = dN[1], dN[0]
36         Bs.append(B) # Store B matrices for stress recovery
37         Ke += B.T @ C @ B * detJ # Accumulate local stiffness
38     return Ke, Bs, detJ
39
40 def build_tensor_dof_mapping(voxel, dx, dy, dz, thickness):
41     nx, ny, nz = voxel.shape # Enforce XYZ indexing convention
42     node_indices = np.arange((nx + 1) * (ny + 1) * (nz + 1)).
43     reshape(nx + 1, ny + 1, nz + 1)
44     dof_tensor = np.zeros((nx + 1, ny + 1, nz + 1, 3), dtype=
45         int)
46     dof_tensor[..., 0], dof_tensor[..., 1], dof_tensor[..., 2]
47     = node_indices * 3, node_indices * 3 + 1, node_indices * 3
48     + 2
49     dof_tensor[nx, :, :, :] = dof_tensor[0, :, :, :]
50     dof_tensor[:, ny, :, :] = dof_tensor[:, 0, :, :]

```

```

41     n1, n2 = dof_tensor[:-1, :-1, :-1, :], dof_tensor[1:, :-1,
42     :-1, :]
43     n3, n4 = dof_tensor[1:, 1:, :-1, :], dof_tensor[:-1, 1:,
44     :-1, :]
45     n5, n6 = dof_tensor[:-1, :-1, 1:, :], dof_tensor[1:, :-1,
46     1:, :]
47     n7, n8 = dof_tensor[1:, 1:, 1:, :], dof_tensor[:-1, 1:, 1:,
48     :]
49     edof_tensor = np.concatenate([n1, n2, n3, n4, n5, n6, n7,
50     n8], axis=-1)
51
52     active_mask = voxel > 0 # Filter out void regions
53     edofMat = edof_tensor[active_mask]
54
55     z_coords = np.linspace(dz / 2, thickness - dz / 2, nz) -
56     thickness / 2.0
57     z_grid = np.broadcast_to(z_coords[None, None, :], (nx, ny,
58     nz)) # Z is the 3rd axis
59     z_active = z_grid[active_mask]
60     return edofMat, z_active, node_indices.size * 3
61
62 def homogenization_plate(voxel, E=2000.0, nu=0.3, thickness
63 =10.0, Nx=1, Ny=1, Nz=1):
64     nx, ny, nz = voxel.shape
65     cell_size = thickness / Nz
66     Lx = Nx * cell_size
67     Ly = Ny * cell_size
68     Lz = thickness
69     dx, dy, dz = Lx / nx, Ly / ny, Lz / nz
70     plate_area = Lx * Ly # Normalization factor for LPS-H
71
72     C = get_isotropic_elasticity(E, nu)
73     Ke, Bs, detJ = compute_element_stiffness(C, dx, dy, dz)
74     edofMat, z_active, total_dofs = build_tensor_dof_mapping(
75     voxel, dx, dy, dz, thickness)
76
77     iK, jK = np.repeat(edofMat, 24, axis=1).flatten(), np.tile(
78     edofMat, (1, 24)).flatten()
79     sK = np.tile(Ke.flatten(), edofMat.shape[0])
80     K = coo_matrix((sK, (iK, jK)), shape=(total_dofs,
81     total_dofs)).tocsr() # Loop-free assembly of global
82     stiffness
83
84     E_macro = np.zeros((len(z_active), 6, 6))
85     E_macro[:, 0, 0], E_macro[:, 1, 1], E_macro[:, 5, 2] = 1.0,
86     1.0, 1.0 # Apply unit membrane strains
87     E_macro[:, 0, 3], E_macro[:, 1, 4], E_macro[:, 5, 5] =
88     z_active, z_active, z_active # Apply unit bending
89     curvatures
90
91

```

```

76     F_ele = sum([np.einsum('ji,kjl->kil', Bs[i], np.einsum('ij,
77     kjl->kil', C, E_macro)) * detJ for i in range(8)]) # Local
        load via tensor contraction
77     F = np.column_stack([np.bincount(edofMat.flatten(), weights
78     =F_ele[:, :, c].flatten(), minlength=total_dofs) for c in
        range(6)]) # Global load assembly
78     active_dofs = np.setdiff1d(np.unique(edofMat), np.unique(
        edofMat)[:3]) # Eliminate rigid body motions
79
80     U = np.zeros((total_dofs, 6))
81     K_active_gpu = csp.csr_matrix(K[active_dofs, :][:,
        active_dofs])
82     F_active_gpu = cp.asarray(F[active_dofs, :])
83     U_active_gpu = cp.zeros((len(active_dofs), 6))
84     M_gpu = csp.diags(1.0 / K_active_gpu.diagonal())
85     streams = [cp.cuda.Stream(non_blocking=True) for _ in range
        (6)] # Initialize concurrent CUDA streams
86     for c in range(6):
87         with streams[c]: # Launch asynchronous GPU solving for
            6 load cases
88             U_col_gpu, _ = cpspla.cg(K_active_gpu, F_active_gpu
           [:, c], M=M_gpu, tol=1e-6, maxiter=5000) # Jacobi
            Preconditioner Conjugate gradient solver on GPU
89             U_active_gpu[:, c] = U_col_gpu
90     for stream in streams:
91         stream.synchronize() # Barrier synchronization
92     U[active_dofs, :] = U_active_gpu.get()
93
94     ABD = np.zeros((6, 6))
95     for i_gp in range(8):
96         Sigma = np.einsum('ij,kjl->kil', C, E_macro - np.einsum
        ('ij,kjl->kil', Bs[i_gp], U[edofMat, :])) # Recover true
        physical stress
97         ABD[0:3, :] += np.sum(Sigma[:, [0, 1, 5], :], axis=0) *
            detJ / plate_area # Extract A and B matrices (0th moment)
98         ABD[3:6, :] += np.sum(Sigma[:, [0, 1, 5], :] * z_active
           [:, None, None], axis=0) * detJ / plate_area # Extract D
            and B* matrices (1st moment)
99     return (ABD + ABD.T) / 2.0 # Symmetrization for Maxwell-
        Betti reciprocity

```

Appendix B Comparison of LVS-H, LPS-H, and the Full-Scale Model

This appendix presents the static comparison results for a representative Lattice-skin Plate Structure with dimensions of $120 \times 120 \times 10$ mm under three modeling strategies: the full-scale finite element model, LPS-H, and LVS-H, as shown in **Figure B1**. To ensure fair comparison, the three models use the same boundary conditions and loading

setup: the upper boundary along the y axis is fully fixed, a displacement load of 1 mm is applied to the lower boundary, and the overall support reaction of the structure is used as the effective stiffness indicator.

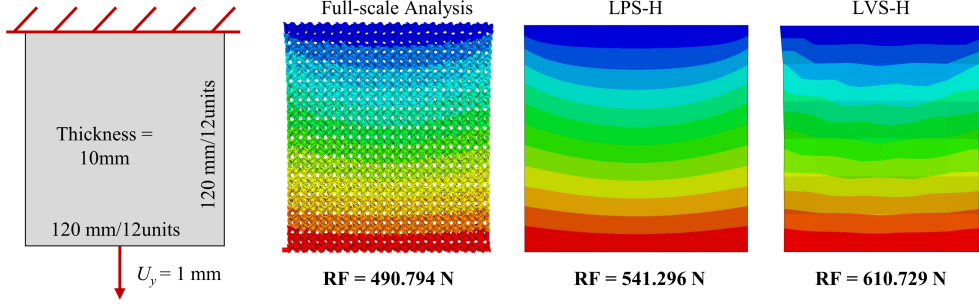


Fig. B1 Comparison of the static responses predicted by the full-scale finite element model, LPS-H, and LVS-H. All three models use the same boundary conditions, with the upper boundary fixed and a 1 mm displacement load applied to the lower boundary, and the support reaction is used to characterize the overall stiffness.

The calculated support reactions of the full-scale finite element model, LPS-H, and LVS-H are 490.794 N, 541.296 N, and 610.729 N, respectively. Taking the full-scale finite element result as the reference, the relative deviation of LPS-H is 10.29%, whereas that of LVS-H reaches 24.43%. This shows that for finite-thickness Lattice-skin Plate Structures, LPS-H can represent the overall response of the real structure under displacement-controlled loading more accurately because it retains the boundary features of the free surfaces through the thickness. By contrast, LVS-H tends to overestimate structural stiffness because of the periodic continuation assumption introduced through the thickness, and therefore predicts a larger support reaction.

It should be noted that the full-scale finite element model is used only for benchmark validation, and its computational cost is much higher than that of the two homogenized models. The model contains more than 5×10^6 elements, requires a high-performance computing platform for solution, and has a peak memory demand of about 240 GB. For Lattice-skin Plate Structures with complex internal topology and finite-thickness truncation effects, direct full-scale 3D simulation requires extensive preprocessing and meshing effort and also consumes substantial computational resources. In comparison, LPS-H retains the key thickness-boundary effects while greatly reducing the computational scale, making it a more efficient substitute model for engineering analysis and structural design.

Acknowledgements. The computations in this paper were run on the Siyuan1 cluster supported by the Center for High Performance Computing at Shanghai Jiao Tong University.

Author contributions. Zhongkai Ji and Dawei Li contributed to the conceptualization of the study. Zhongkai Ji contributed to the methodology, validation, and original draft preparation of the manuscript. Dawei Li contributed to funding acquisition,

project administration, and manuscript review and editing. Yong Zhao contributed to the methodology, supervision, and manuscript review and editing. Wenhe Liao contributed to resources and supervision. Dawei Li (ldw@njust.edu.cn) and Yong Zhao (yongzhao@sjtu.edu.cn) are co-corresponding authors of this paper.

Funding. This work was supported by the National Natural Science Foundation of China (Grant No. 52575292).

Data availability. The data used in this study are available at <https://github.com/TopJournals/ThinWalledHomogenization>.

Declarations

Conflict of interest. The authors declare that they have no known competing financial interests or personal relationships that could have appeared to influence the work reported in this paper.

Replication of results. The code is available at <https://github.com/TopJournals/ThinWalledHomogenization>.

References

- Andreassen, E., Andreassen, C.S.: How to determine composite material properties using numerical homogenization. *Computational Materials Science* **83**, 488–495 (2014) <https://doi.org/10.1016/j.commatsci.2013.09.006>
- Bishara, D., Xie, Y., Liu, W.K., Li, S.: A State-of-the-Art Review on Machine Learning-Based Multiscale Modeling, Simulation, Homogenization and Design of Materials. *Archives of Computational Methods in Engineering* **30**(1), 191–222 (2023) <https://doi.org/10.1007/s11831-022-09795-8>
- Bayat, M., Zinovieva, O., Ferrari, F., Ayas, C., Langelaar, M., Spangenberg, J., Salajeghe, R., Poullos, K., Mohanty, S., Sigmund, O., Hattel, J.: Holistic computational design within additive manufacturing through topology optimization combined with multiphysics multi-scale materials and process modelling. *Progress in Materials Science* **138**, 101129 (2023) <https://doi.org/10.1016/j.pmatsci.2023.101129>
- Cai, Y., Xu, L., Cheng, G.: Novel numerical implementation of asymptotic homogenization method for periodic plate structures. *International Journal of Solids and Structures* **51**(1), 284–292 (2014) <https://doi.org/10.1016/j.ijsolstr.2013.10.003>
- Ding, W.: An easy-to-use univariate mapping-based method for multi-material topology optimization with implementation in MATLAB. *Structural and Multidisciplinary Optimization* **68**(3), 48 (2025) <https://doi.org/10.1007/s00158-025-03983-3>
- Dong, G., Tang, Y., Zhao, Y.F.: A 149 line homogenization code for three-dimensional cellular materials written in matlab. *Journal of Engineering Materials and Technology* **141**(1), 011005 (2019) <https://doi.org/10.1115/1.4040555>

- Gao, J., Cao, X., Xiao, M., Yang, Z., Zhou, X., Li, Y., Gao, L., Yan, W., Rabczuk, T., Mai, Y.-W.: Rational designs of mechanical metamaterials: Formulations, architectures, tessellations and prospects. *Materials Science and Engineering: R: Reports* **156**, 100755 (2023) <https://doi.org/10.1016/j.mser.2023.100755>
- Han, Z., Wei, K.: Multi-material topology optimization and additive manufacturing for metamaterials incorporating double negative indexes of Poisson's ratio and thermal expansion. *Additive Manufacturing* **54**, 102742 (2022) <https://doi.org/10.1016/j.addma.2022.102742>
- Ji, Z., Li, D., Xie, Y.M., Zhao, Y., Liao, W.: Design and optimization of TPMS-based heterogeneous metastructure for controllable displacement field. *Thin-Walled Structures* **208**, 112784 (2025) <https://doi.org/10.1016/j.tws.2024.112784>
- Khan, N., Riccio, A.: A systematic review of design for additive manufacturing of aerospace lattice structures: Current trends and future directions. *Progress in Aerospace Sciences* **149**, 101021 (2024) <https://doi.org/10.1016/j.paerosci.2024.101021>
- Qiao, K., Xu, X., Guo, S.: Numerical Implementation of Variational Asymptotic Homogenization Method for Periodic Plate Structures. *International Journal of Aeronautical and Space Sciences* **22**(1), 64–78 (2021) <https://doi.org/10.1007/s42405-020-00285-4>
- Sigmund, O.: A 99 line topology optimization code written in matlab. *Structural and Multidisciplinary Optimization* **21**(2), 120–127 (2001) <https://doi.org/10.1007/s001580050176>
- Sun, C., Li, D., Liao, W., Liu, T.: Rigid-flexible interlocked metastructures enable conformal stealth. *Science Advances* **11**(49), 7870 (2025) <https://doi.org/10.1126/sciadv.aeb7870>
- Wang, P., Guo, J., Yuan, Y., Li, C., Wang, Y., Guang, M., Yan, J., Liu, W., Sun, Z.: Bio-inspired vertex-offset lattice metamaterials with enhanced stress stability and energy absorption. *Thin-Walled Structures* **210**, 113060 (2025) <https://doi.org/10.1016/j.tws.2025.113060>
- Woldseth, R.V., Sigmund, O., Jensen, P.D.L.: An 808 line phasor-based dehomogenisation matlab code for multi-scale topology optimisation. *Structural and Multidisciplinary Optimization* **67**(12), 205 (2024) <https://doi.org/10.1007/s00158-024-03880-1>
- Yang, Y., Wang, L., Zhai, X., Chen, K., Wu, W., Zhao, Y., Chen, F., Liu, L., Fu, X.-M.: Guided diffusion for fast inverse design of voxel-based mechanical metamaterials. *Smart Materials in Manufacturing* **4**, 100129 (2026) <https://doi.org/10.1016/j.smmf.2026.100129> arXiv:2401.13570 [cs]

- Yi, S., Xu, L., Cheng, G., Cai, Y.: FEM formulation of homogenization method for effective properties of periodic heterogeneous beam and size effect of basic cell in thickness direction. *Computers & Structures* **156**, 1–11 (2015) <https://doi.org/10.1016/j.compstruc.2015.04.010>
- Zhou, B.: An efficient method to estimate the structural stiffness of large periodic floating plate-like structures. *Ocean Engineering* **335**, 121636 (2025) <https://doi.org/10.1016/j.oceaneng.2025.121636>
- Zhou, M., Sigmund, O.: Complementary lecture notes for teaching the 99/88-line topology optimization codes. *Structural and Multidisciplinary Optimization* **64**(5), 3227–3231 (2021) <https://doi.org/10.1007/s00158-021-03004-z>
- Zheng, X., Zhang, X., Chen, T.-T., Watanabe, I.: Deep learning in mechanical metamaterials: From prediction and generation to inverse design. *Advanced Materials* **35**(45), 2302530 (2023) <https://doi.org/10.1002/adma.202302530>
- Zhang, D., Zhai, X., Liu, L., Fu, X.-M.: An optimized, easy-to-use, open-source GPU solver for large-scale inverse homogenization problems. *Structural and Multidisciplinary Optimization* **66**(9), 207 (2023) <https://doi.org/10.1007/s00158-023-03657-y>